Key Words:
MST
Permanganate
Peroxide

Retention:
Permanent

Transmission Electron Microscopy Analyses of Strontium and Actinide-Bearing Monosodium Titanate and Permanganate Treatment Solids

Nancy L. Dietz, Jeffrey A. Fortner
Argonne National Laboratory
Chemical Technology Division
Argonne, IL 60439

Zurong Dai, John P. Bradley
Formerly with: The Georgia Institute of Technology, Atlanta, GA
Presently at: Lawrence Livermore National Laboratory
Livermore, CA 94551

Martine C. Duff, David T. Hobbs and Samuel D. Fink
Westinghouse Savannah River Company
Savannah River Site
Aiken, SC 29808

SEPTEMBER 19, 2002

Westinghouse Savannah River Company
Savannah River Site
Aiken, SC 29808

SAFETY • RESPONSIBILITY • SECURITY
SRS
SAVANNAH RIVER SITE

Prepared for the U.S. Department of Energy Under
Contract Number DE-AC09-96SR18500

WSRC-TR-2002-00363, Revision 0

Key Words:
MST
Permanganate
Peroxide

Retention:
Permanent

Transmission Electron Microscopy Analyses of Strontium and Actinide-Bearing Monosodium Titanate and Permanganate Treatment Solids

Nancy L. Dietz, Jeffrey A. Fortner
Argonne National Laboratory
Chemical Technology Division
Argonne, IL 60439

Zurong Dai, John P. Bradley
Formerly with: The Georgia Institute of Technology, Atlanta, GA
Presently at: Lawrence Livermore National Laboratory
Livermore, CA 94551

Martine C. Duff, David T. Hobbs and Samuel D. Fink
Westinghouse Savannah River Company
Savannah River Site
Aiken, SC 29808

SEPTEMBER 19, 2002

Westinghouse Savannah River Company
Savannah River Site
Aiken, SC 29808

SAFETY • RESPONSIBILITY • SECURITY
SRS
SAVANNAH RIVER SITE

Prepared for the U.S. Department of Energy Under
Contract Number DE-AC09-96SR18500

REVIEWS AND APPROVALS

Martine C. Duff 9/19/02

M. C. Duff, Author, Waste Processing Technology Date

D.T. Hobbs 9/23/02

D. T. Hobbs, Author, Waste Processing Technology Date

M. Tosten 9-28-02

M. Tosten, Design Check, Materials Technology Date

Samuel D. Fink 9-30-02

S. D. Fink, Level 4 Manager and TFA Lead, Waste Processing Technology Date

10/3/02

H. D. Harmon, SPP Technology Development Manager, Process Engineering Date

for Harry D. Harmon 10/1/02

J. T. Carter, Director of Engineering, SWPF Date

James C. Marshall for WLT 10/3/02

W. L. Tamosaitis, Manager, Waste Processing Technology Date

W D Clark 10/3/02

W. D. Clark, Jr., DOE-SR, Technical Support Manager Date

TABLE OF CONTENTS

LIST OF FIGURES

LIST OF TABLES

ACRONYMS AND ABBREVIATIONS

Al	Aluminum
ANL	Argonne National Laboratory
CMT	Chemical Materials Technology
Cs	Cesium
Cu	Copper
EDS	Energy Dispersive X-ray emission Spectroscopy
EELS	Electron Energy Loss Spectroscopy
FFT	Fast Fourier transform
GaTech	Georgia Institute of Technology
GIF	Gatan Image Filter
HLW	High Level Waste
H_2O_2	Hydrogen Peroxide
ICP-MS	Inductively-Coupled argon Plasma Mass Spectrometry
Mn	Manganese
MST	Monosodium Titanate
Na	Sodium
$Na_4Mn_{14}O_{27}•9H_2O_{(s)}$	Sodium Birnessite
O	Oxygen
OH^-	Hydroxide
Pu	Plutonium
Q	Momentum Transfer
SAED	Selected Area Electron Diffraction
S	Sulfur
SEM	Scanning Electron Microscopy
Si	Silicon
Sr	Strontium
SRTC	Savannah River Technology Center
TEM	Transmission Electron Microscopy
Ti	Titanium
U	Uranium
XAFS	X-ray Absorption Fine-Structure spectroscopy
XANES	X-ray Absorption Near-Edge Structure spectroscopy
WSRC	Westinghouse Savannah River Company

1.0 ABSTRACT

Nearly 130 million L of high-level waste (HLW, the radioactive waste product associated with the dissolution of spent nuclear fuel rods for the recovery of weapons grade material) await disposition at the Savannah River Site (SRS). The current design for the Salt Processing Facility at the SRS includes use of monosodium titanate (MST) to remove and concentrate the strontium and actinides (uranium, plutonium and neptunium) from HLW salt solutions. However, the River Protection Program (RPP) at the Hanford Site in Washington State proposes use of permanganate addition for strontium and actinide removal from Hanford HLW.

X-ray diffraction studies indicate MST and the permanganate solids are amorphous. The mechanism(s) by which strontium and the actinides are removed during permanganate treatment or during the addition of MST in SRS HLW solutions are not known. Studies with actual and simulant wastes show that removal of these radionuclides during permanganate treatment occurs during the precipitation of brownish-black manganese-rich solids.[1, 2] However, the structures of the manganese solids that form in SRS HLW treatment studies have not been characterized.

Transmission Electron Microscopy (TEM) analyses were conducted on MST and permanganate-treatment sorbent materials produced at the Westinghouse Savannah River Company - Savannah River Technology Center (WSRC SRTC). Researchers at Argonne National Laboratory (ANL) performed studies on actinide-bearing samples. Personnel from Georgia Institute of Technology (GaTech) performed measurements on several non-radioactive samples. This work increases the fundamental understanding of the strontium and actinide sorbent interactions. This information also complements a previous XAFS analysis of the solids.

The analyses performed included lattice fringe imaging, selected area electron diffraction (SAED) for crystal structure determination, energy dispersive X-ray emission spectroscopy (EDS), electron energy loss spectroscopy (EELS) for elemental composition in addition to some scanning electron microscopy (SEM) analyses.

The MST particles consist of an amorphous or nanocrystalline interior surrounded by highly distorted sheets of crystalline “fringes”. The outer fibrous portion of the MST has a high degree of curvature, indicating some lack of order in the crystal structure. The lack of structural order may result from the presence of interlayer water. The outer-fringed layer has a sheet-like structure and varies in thickness from approximately 200 to 500 nm. The interior of the MST particles is an amorphous (i.e., glass-like) or nanocrystalline material. The EELS analyses with the MST samples indicate that the titanium in MST is octahedrally coordinated. Diffraction analyses indicate that the composition of the fringe material is unique and does not resemble that of known titanate structures.

- The analyses indicate that the strontium from HLW simulants sorbs to the outer fibrous material on the MST particles.

- We could not detect the actinides by imaging and by TEM-based spectroscopic techniques. This suggests the actinides are heterogeneously distributed on the MST and that the samples chosen did not contain sufficient concentrations of actinides for TEM analyses.
- The permanganate-treatment material consisted of small (~200 nm diameter or less) nanocrystalline manganese-containing particles, along with larger aluminum oxide particles. There are two types of morphologies of manganese oxide particles: hexagonal-shaped particles and fibrous particles. The elemental make of these particles is nearly identical. The EELS method did not detect actinides indicating their localized concentrations fell below the nominal detection limit of 0.1 atomic percent.

- The method of MST synthesis could be optimized to improve strontium removal, and possibly actinide removal. This optimization would allow the process to meet performance requirements for strontium and actinide removal with less material. We recommend additional studies related to improving the synthesis.

2.0 INTRODUCTION

Treatment of High-Level Radioactive Waste at the Savannah River Site includes the use of MST or, potentially, manganese (Mn) oxide sorbents for the removal of selected actinides (plutonium, uranium and neptunium). Little is known about the structure MST. Results from X-ray diffraction (XRD) studies indicate MST is highly amorphous and scanning electron microscopy studies show that the particles are spherical (snowball-like) with a typical size range of 5 to 12 μm.[3] The MST may possess a layered structure like that of the more crystalline solid called sodium nonatitanate.[4] Additionally, little is known about the structure of the black precipitate that forms upon permanganate reduction in HLW salt solutions. XDR studies indicate the Mn solids are amorphous.[5]

2.1 Sorbent Reactivity and Mechanism are Related to Sorbent Structure

The affinity of Mn oxides for dissolved ions is often related to structure. For the Mn oxides, the basic building blocks are Mn octahedra (**Figure 2.1**), which can link via three orientations to form larger structures. Few sorption studies with Mn oxides discern between the various types of Mn oxide structures and many simply refer to the solids as being manganese oxide. Several Mn oxides exist with similar elemental stoichiometries but they can have different structural arrangements of their Mn octahedra.[6, 7]

For example, the tunnel-structured manganates consist of mainly corner-sharing Mn octahedra (**Figure 2.1**). These solids have sorption capacities that often exceed that of zeolitic materials and their linkages of the Mn octahedra result in the formation of long tunnels, which can be size-excluding to some ions.[8] However, these solids often have low affinities for plutonium (Pu) and strontium (Sr) relative to cesium (Cs) and other radionuclides such as americium.[9]

Layered manganates have primarily edge-linked Mn octahedra and, until recently, the structures of these layered manganates were unknown (**Figure 2.1**).[10] They have a lamellar structure of Mn octahedral layers with interlayer water and hydroxyl groups. In nature, the layered Mn oxides tend to be poorly crystalline with small particle size and high surface areas per volume. Layered structures often contain interlayer cations, which can be displaced by other sorbing ions such as the actinides. For titanates, enhanced sorption behavior due to a layered (versus a tunnel) structure also occurs—particularly with the layered titanates investigated for radionuclide sorption from SRS HLW.[11] Layered structures may exhibit corner-sharing behavior, which gives them a more three-dimensional structure than the two-dimensional structures that exist for solids with only edge-linked titanium (Ti) (or Mn) octahedra. However, little structural information (such as whether the Ti is mostly present as Ti octahedra or Ti tetrahedra) exists for the titanate sorbents with high affinities for radionuclides.

Basic Building Blocks of Mn(IV) Oxides

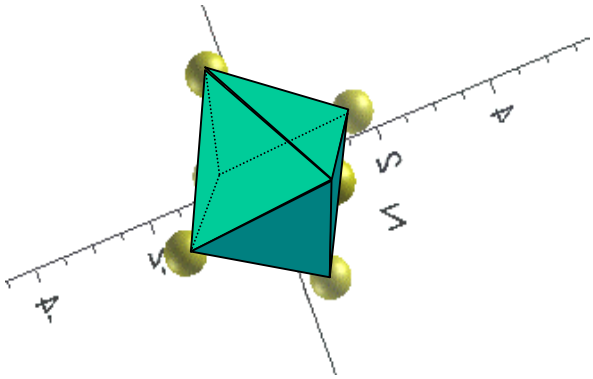

A. One Mn(IV) octahedron with 6 first shell oxygens at 1.9Å in octahedral symmetry

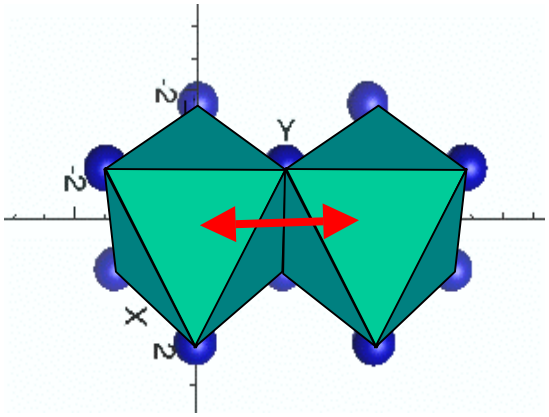

C. Two Mn(IV) octahedra sharing 2 oxygens. Termed "edge" sharing, Mn-Mn distance 2.85 Å

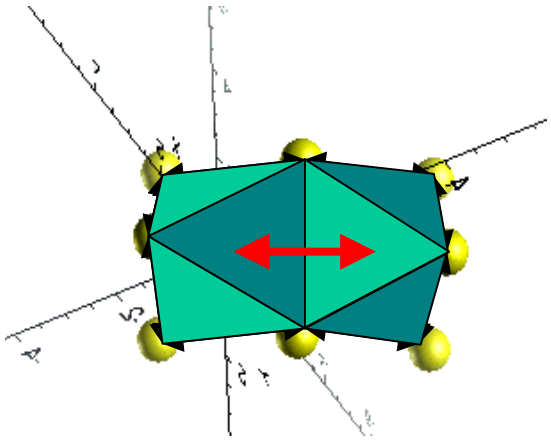

B. Two Mn(IV) octahedra sharing 3 oxygens. Termed "face" sharing, Mn-Mn distance 2.5 Å

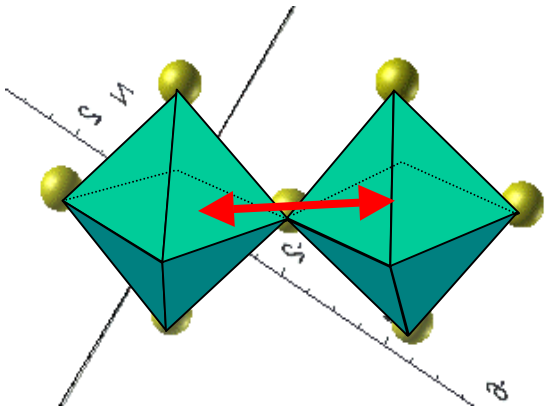

D. Two Mn(IV) octahedra sharing 1 oxygen. Termed "corner" sharing, Mn-Mn distance 3.8 Å

Figure 2.1 Basic building blocks of Mn(IV) oxides. Similar arrangements also exist with Ti octahedra. Edge- and corner-sharing Mn octahedra are the most common linkages observed in naturally occurring Mn oxides. Red arrows point to the distance between the Mn atoms in the linked Mn octahedra.

NOTE: Due to document format problems, the figure shown above is not a complete reproduction of that presented in the original report document.

2.2 Use of TEM Methods to Characterize Actinide-Bearing Sorbent Materials

The microstructure, crystal structure, topography, and composition of a material can be characterized using Transmission Electron Microscopy (TEM) methods. As an imaging device, the TEM can provide atomic plane imaging and, with X-ray and electron spectroscopy devices, it can provide elemental analyses with relatively high spatial resolution and high analytical sensitivity. Electron images with magnifications of 1000x to 1,000,000x can be obtained for radioactive samples. The TEM techniques have been used to characterize Mn oxides[12, 13, 14, 15] and to a lesser degree, the titanates.[16] TEM imaging of particle morphology can often provide information to help infer the crystal structure. However, diffraction techniques are clearly more definitive.

Electron diffraction patterns can help identify crystal structure, which can be used to determine for example, whether Mn octahedra are corner or edge linked. The use of selected area electron diffraction (SAED) techniques, which provide spatially-resolved diffraction analyses can be particularly helpful when the bulk sample does not possess enough long range crystallinity (i.e., order) or similar orientations to exhibit a prominent diffraction pattern. The SAED techniques can in many cases, provide diffraction information for single particles.

The energy dispersive spectroscopy (EDS) capability of TEM can identify elements present at the ~1% level. The electron energy loss spectroscopy (EELS) techniques provide light element detection [e.g., boron, carbon, nitrogen, oxygen (O)] and chemical information (e.g., oxidation state). The EELS techniques are similar to that of X-ray absorption near-edge structure (XANES) spectroscopic techniques in that they provide information on the local coordination environment of the element of interest. Hard (high) energy X-ray spectroscopic techniques are usually not usually performed under vacuum. The EELS techniques are conducted under vacuum, which facilitates the detection of soft X-rays, such as those for the light atoms [O, aluminum (Al), silicon (Si), etc…] in addition to the detection of the actinides at their M absorption edges.

Due to the low fluorescence yields observed at low edge energies, the sensitivity of the EELS method for detection of the d-transition and actinide elements is much diminished relative to that of techniques conducted at higher energies. In other words, the EELS techniques typically require much higher actinide loadings than that of higher (i.e., hard X-ray) energy XANES techniques. The case is most extreme for the actinides.[a] However, EELS can be more advantageous than conventional XANES studies because it is a highly spatially resolved technique. For example, one can optimize EELS detection capabilities by selecting small sample regions that are enriched in actinides, such as those areas on samples with Pu colloids.

[a] Actinides and the heavy elements (such as the d-transition elements) have several absorption edges in the sub keV to high keV range, but the fluorescence yields for the actinides are lower at low energies (for example at the uranium (U) M_5 edge at 3.552 keV) than the fluorescence yields for the actinides at higher edge energies (for example at the U L_3 edge at 17.166 keV or the U K-edge near 100 keV).

2.3 Experimental Objectives

Prior studies included X-ray absorption fine-structure (XAFS) spectroscopy measurements on MST and Mn oxide solids reacted with HLW salt solutions doped with actinides.[5, 17, 18] This study attempted to gain complementary information on the preferred binding sites, the actinide structure and distribution at these sites, and the sorbent microstructure with the goal of understanding how these materials remove actinides from HLW streams. To this end, Argonne National Laboratory (ANL) provided TEM analyses including lattice fringe imaging, SAED, EDS and EELS for four radioactive sorbent materials supplied by SRTC. Georgia Institute of Technology (GATech) performed initial TEM analyses as a feasibility study for these techniques.

3.0 MATERIALS AND EXPERIMENTAL METHODS

3.1 Sample Preparation and TEM Analyses at Georgia Institute of Technology

As part of a feasibility study, SRTC personnel supplied air-dried sub-samples of untreated and Sr-treated MST to GaTech for TEM analyses. The Sr-loaded MST sample (SrMST1) had a Sr loading of 9000 mg Sr kg^{-1} as described in Duff et al. (2001).[17] The sample preparation for transmission electron microscopic examination involved embedding in EMBED-812 resin followed by thin-sectioning using ultramicrotomy. Ultramicrotomy is a mechanical method of producing thin sections that does not depend on material sputtering rate or dissolution behavior. Instead, thin sections are sliced from the sample using a diamond knife. As each section is produced, it is pushed off the knife-edge by the next section. Sections float on water where they are collected onto an electron transparent carbon substrate. Interfaces are better retained in thin sections prepared by ultramicrotomy than those prepared by sputtering (ion milling) or chemical etching.

Section thickness equaled 50 to 70 nm. Personnel used a 200 keV Hitachi HF2000 field emission and 400 keV JOEL 4000EX instruments using brightfield and darkfield imaging, SAED, lattice-fringe imaging, and EDS analyses.

3.2 Samples Selected for TEM Analyses at ANL

The SRTC personnel provided a non-radioactive sample of Mn oxide for a feasibility test of the ultramicrotomy and analysis with TEM. This sample came from treating a 11.6 M Na^+ salt solution (i.e., a Tank 36H salt simulant solution) using 0.01 M permanganate and 0.045 M H_2O_2. The salt solution contained 8 M NaOH, 1.5 M $NaNO_3$, 1.7 M $NaNO_2$, and 0.41 M $NaAl(OH)_4$.

The SRTC staff provided ANL with samples of MST and permanganate-treated solids as listed in **Table 3.1**. Preparation of the MST samples (A1, C1, and UMST1) followed the description in Duff et al. (2001).[18] Sample A1 contains Pu that added as Pu(IV) whereas Sample C1 contains Pu initially added as Pu(VI). Sample UMST1 contains U added as U(VI). Preparation of the Pu-loaded Mn oxide [added as Pu(IV)] followed the description for the Test 14 sample using 0.0025 M permanganate and 0.045 M hydrogen peroxide (H_2O_2) [as listed in Duff et al. (2002)].[5] This sample preparation occurred in 5.6 M sodium (Na) salt solution. Personnel used the low permanganate concentration in hopes of producing a solid with a high Pu loading as discussed in Duff et al. (2002).[5]

3.3 Ultramicrotomy at ANL

Personnel prepared samples for ultramicrotomy by embedding a small quantity of each sorbent in an embedding resin. This study used a lower viscosity resin consisting of a methacrylate and styrene monomer blend, which was different than the epoxy-based resin that was used by Georgia Tech. Personnel prepared two embedded samples of each material using each resin and evaluated in the TEM. These sections remained intact with relatively uniform thickness and minimal sectioning artifacts.

Sections were produced using a Reichart Ultracut E Ultramicrotome. Personnel obtained sections at several sectioning speeds and section thicknesses to evaluate sectioning parameters in the TEM and to subsequently provide the best sections for each TEM technique. For example, the thin sections provide the best lattice images and EELS analyses, whereas thick sections provide the best EDS analyses. Personnel prepared sections with thicknesses ranging from approximately 30 to 100 nm onto a 3-mm carbon-coated copper (Cu) grid support for TEM analyses.

Table 3-1 Materials supplied to ANL for examination.

WSRC Sample ID	Sample Description	Actinide Concentration*
UMST1	U/MST	7,500 mg U kg^{-1}
A1	$Pu^{239/240}$(IV)/MST	553 mg Pu kg^{-1}
C1	$Pu^{239/240}$(VI)/MST	9,960 mg Pu kg^{-1}
Pu-4B-4h	$Pu^{239/240}$/Manganese Oxide	2,920 mg Pu kg^{-1} (estimated)
Manganese Oxide	Manganese Oxide	Non-radioactive

* Amounts based on inductively-coupled argon plasma mass spectrometry (ICP-MS) analyses conducted by SRTC.[5, 17, 18]

3.4 TEM/SAED/EDS/EELS/SEM Analyses at ANL

The TEM analyses used a JEOL 2000FX TEM equipped with an iXRF EDS spectrometer and a Gatan GIF/EELS system. The TEM was operated at 200 keV. Personnel obtained lattice plane images at a magnification of 500,000x. They recorded most images on electron microscope film, with the remaining images recorded with a slow scan charged coupled device (CCD) camera. Recording of electron diffraction patterns used either film or a CCD camera. In the former case, personnel calibrated the diffraction camera length, and obtained the experimental d-spacings using the relation:

$$d = \lambda L/R, \quad (1)$$

where d is the d-spacing, λ is the electron de Broglie wavelength, R is the measured diffraction radius, and L is the calibrated camera length. For the CCD camera, personnel calibrated the camera pixel size in momentum transfer, Q, and obtained the d-spacing using the relation:

$$d = 2\pi/Q. \quad (2)$$

Personnel measured the lattice fringe spacing directly from the electron microscope negative. They scanned the negatives and subsequently processed using Adobe Photoshop© software for incorporation into this report.

The EDS spectra used an acquisition time of 100 seconds at a count rate of approximately 1500 to 2000 counts per second.

The EELS spectra collection occur in diffraction mode using a small camera length (~10 to 20 cm). Energy dispersion occurred with either 1 eV per channel to search for actinide N- and M-edges or 0.2 eV per channel for high-resolution of Ti, Mn, and O near-edge fine structure. The signals for energy loss below 800 eV proved detector-limited, and the instrument operated with the CCD camera near saturation. The spectra presented in this report include background-subtraction and correction for multiple scattering following a standard procedure.[19] The signals for energy loss above 3 keV (e.g., the actinide M-edge region) proved count-limited, and the detector operated somewhat below saturation, with spectra collected at 100-second intervals. Personnel used both normal spectroscopy and second-difference spectroscopy.[20] The latter method minimizes artifacts arising from channel-to-channel gain variations and dark current subtraction.

Personnel prepared the SEM sample by smearing the wet sample over the surface of a polished aluminum stub. The smear occurred by dragging the edge of a microscope slide over the sample while applying pressure. This created a very thin layer of sample. Personnel air-dried the sample and then lightly coated with evaporated carbon (to make the sample conductive). Researchers used a Topcon ABT-60 SEM to obtain secondary electron images at 20 keV.

All calibrations (of magnification, diffraction, EDS, and EELS spectrometer dispersion) used a Si(111) crystal-based standard (MAG*I*CAL, from Norrox Scientific). **Table 3-2** shows the diffraction data for the internal standard (alumina) used during the SAED analyses. Calibration records are maintained by the Chemical Materials Technology (CMT) Division as part of a quality assurance program consistent with DOE/RW-0333P, Rev. 10.

Table 3-2 Diffraction from embedded alumina particles as an internal standard.

Measured d (Å)	$Al_2O_{3-\delta}$ JCPDS80-956
2.75	2.79, 2.80
2.33	2.37, 2.38
1.92	1.96, 1.98
1.49	1.51, 1.52
1.38	1.39, 1.40
0.99	
0.88	

4.0 RESULTS

4.1 TEM Characterization of Untreated MST and Sr-loaded MST

The TEM analyses with untreated MST indicate the sample has two prominent morphological populations of titanate material (**Figure 4.1a** and **4.1b**). The first population includes a very fine fibrous crystalline surface material while the second consists of amorphous material (compare the SAED patterns in the insets for **Figure 4.1a** and **4.1b**). The SAED analyses with the fibrous MST material produce the peak intensities shown in **Table 4.1**, which do not match any known Ti phases. The basal spacing for the fibrous component of the MST is approximately 0.63 nm (**Figure 4.1c**). The basal spacing measurements and electron diffraction peak intensity determinations prove very similar for the untreated MST and the Sr-loaded MST—suggesting the addition of Sr^{2+} (or HLW simulant solution) does not change the MST structure or induce crystallization of the amorphous portion of the MST.

The TEM studies with Sr-sorbed MST indicate that addition of Sr to the MST (sample SrMST1) does not induce morphological changes in the MST (i.e., the added Sr^{2+} from the salt solution does not facilitate the crystallization of the MST). The added Sr is only observed (using EDS analyses, see **Figures 4.2** and **4.3**) on the fibrous portions of the MST. High levels of Al, Si, Ti and Na are also observed in the EDS spectra. Copper is present due to the Cu sample grid. Little detectable Sr existed on the amorphous glass-like interior regions of the particles. The thickness of the fibrous surface MST material did not change upon addition of Sr to the MST. Additionally, the SAED pattern for the Sr-sorbed fibrous component of the MST (data not shown) also remained unchanged—suggesting that the added Sr does not facilitate a conversion of the amorphous component to a more crystalline material. Some titanate minerals can change structure when a large amount of a new cation (such as Sr^{2+}) adds to the structure.[21] However, MST appears to resist structural changes upon addition of Sr^{2+} in the high Na^{+} matrix.

Table 4-1 Electron diffraction from exterior fringes of untreated MST specimen—data from Z. Dai and J. P. Bradley.

d-spacing (Å)
3.656 to 3.144 (broad)
2.577
2.312 to 2.182 (broad)
1.894
1.497
1.404
1.173
0.945

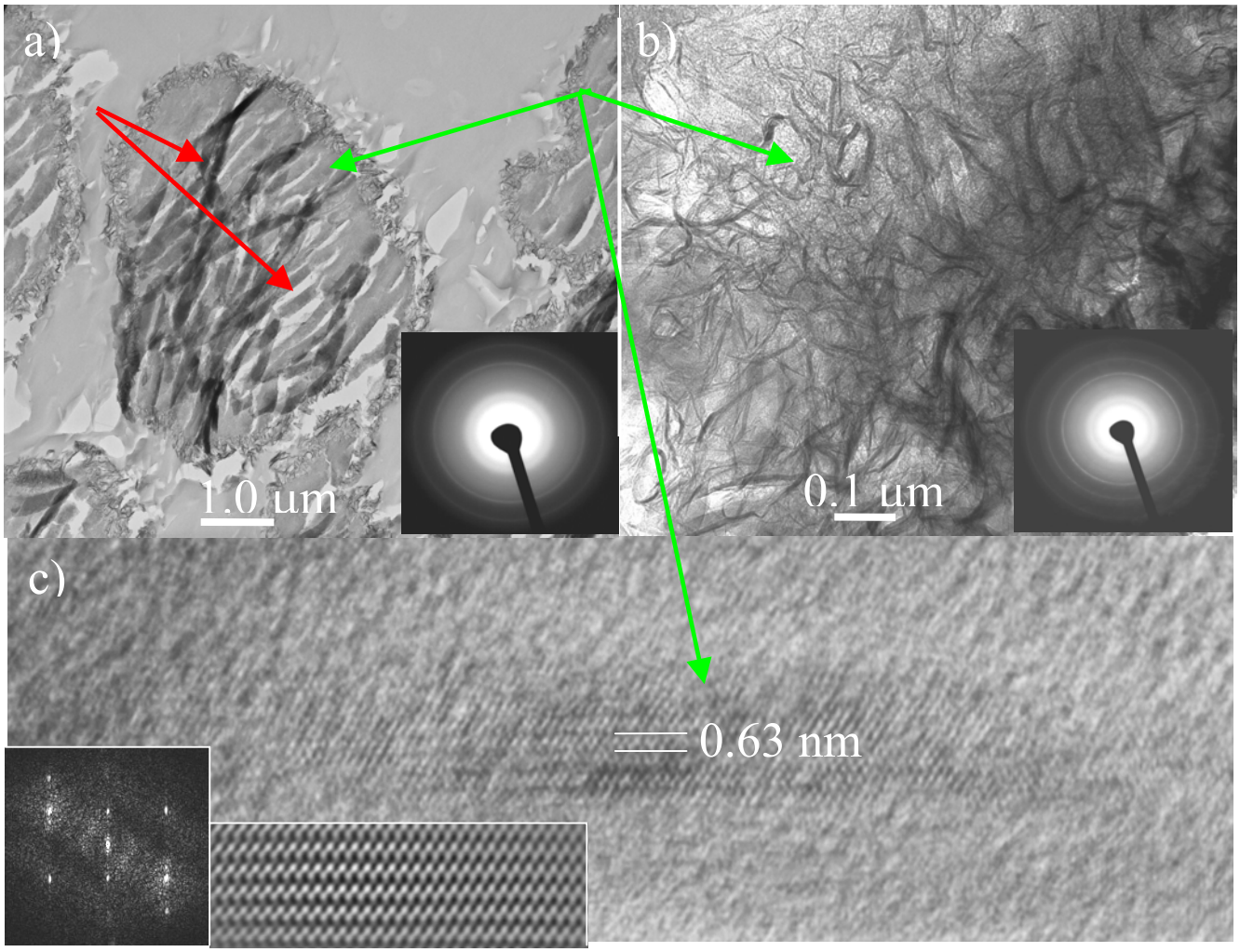

Figure 4.1 Low magnification brightfield TEM images.[b]

[b] The images show a) the typical morphology of MST with corresponding SAED pattern, b) higher magnification brightfield image showing fibrous material (green arrows) at the edges of the grain, and c) high resolution TEM image of a single fiber-like crystal shown in b). Inset at far left corner of c) is a fast Fourier transform (FFT) of the lattice image whereas the inset at left bottom of c) is a Fourier filtered image of the lattice image. The red arrows denote amorphous material. The thick black lines are evidence of particle "shattering", which are the presence of MST shards displaced during sectioning.

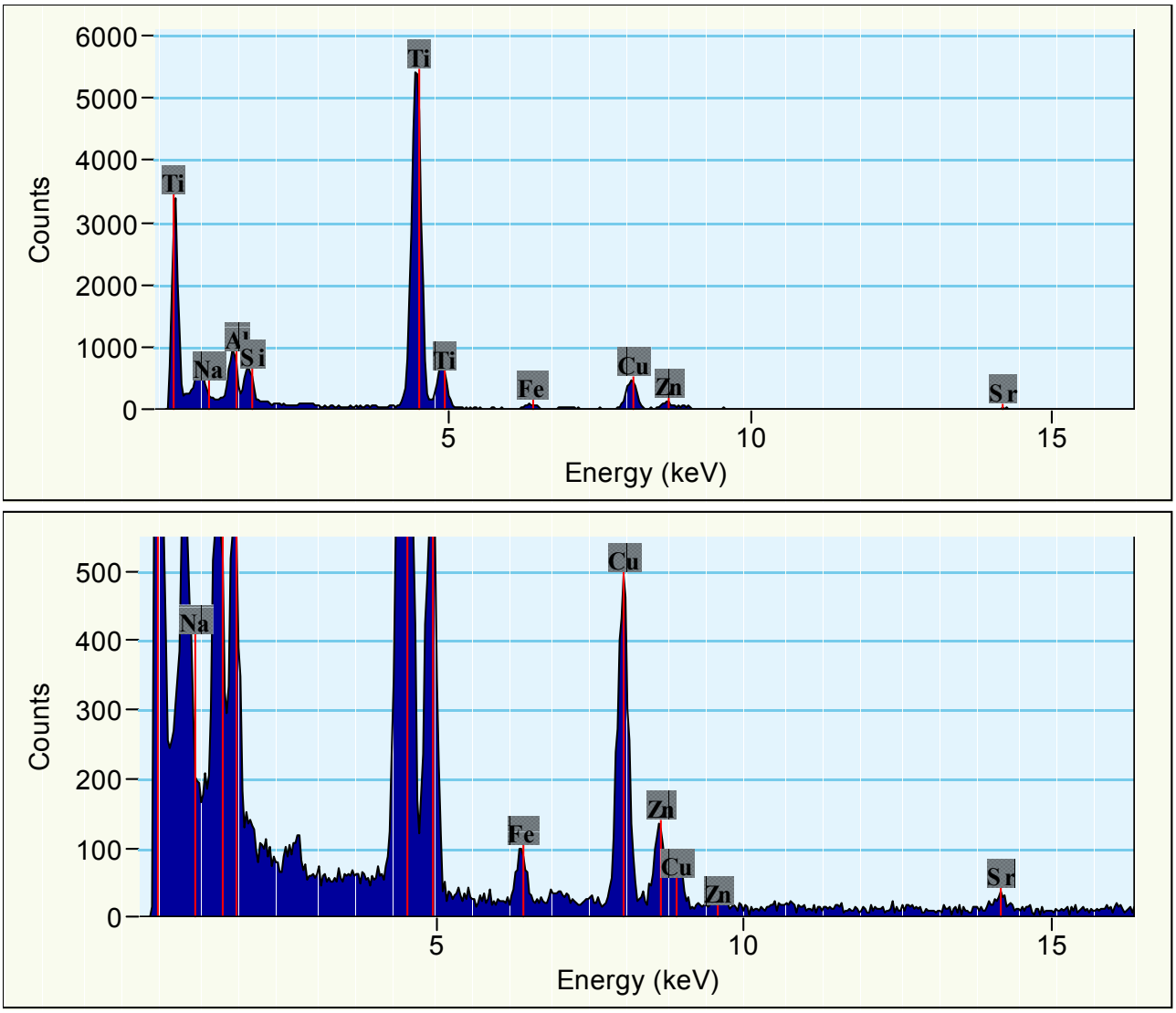

Sr-MST1 Edge area

Figure 4.2 EDS spectra taken on the fringe edges of the Sr-loaded MST showing the presence of small amounts of Sr, in addition to larger amounts of Ti, Al, Na, Si, Fe and Zn. (The Cu peaks come from the Cu in the sample grid.)

NOTE: Due to document format problems, the figure shown above is not a complete reproduction of that presented in the original report document.

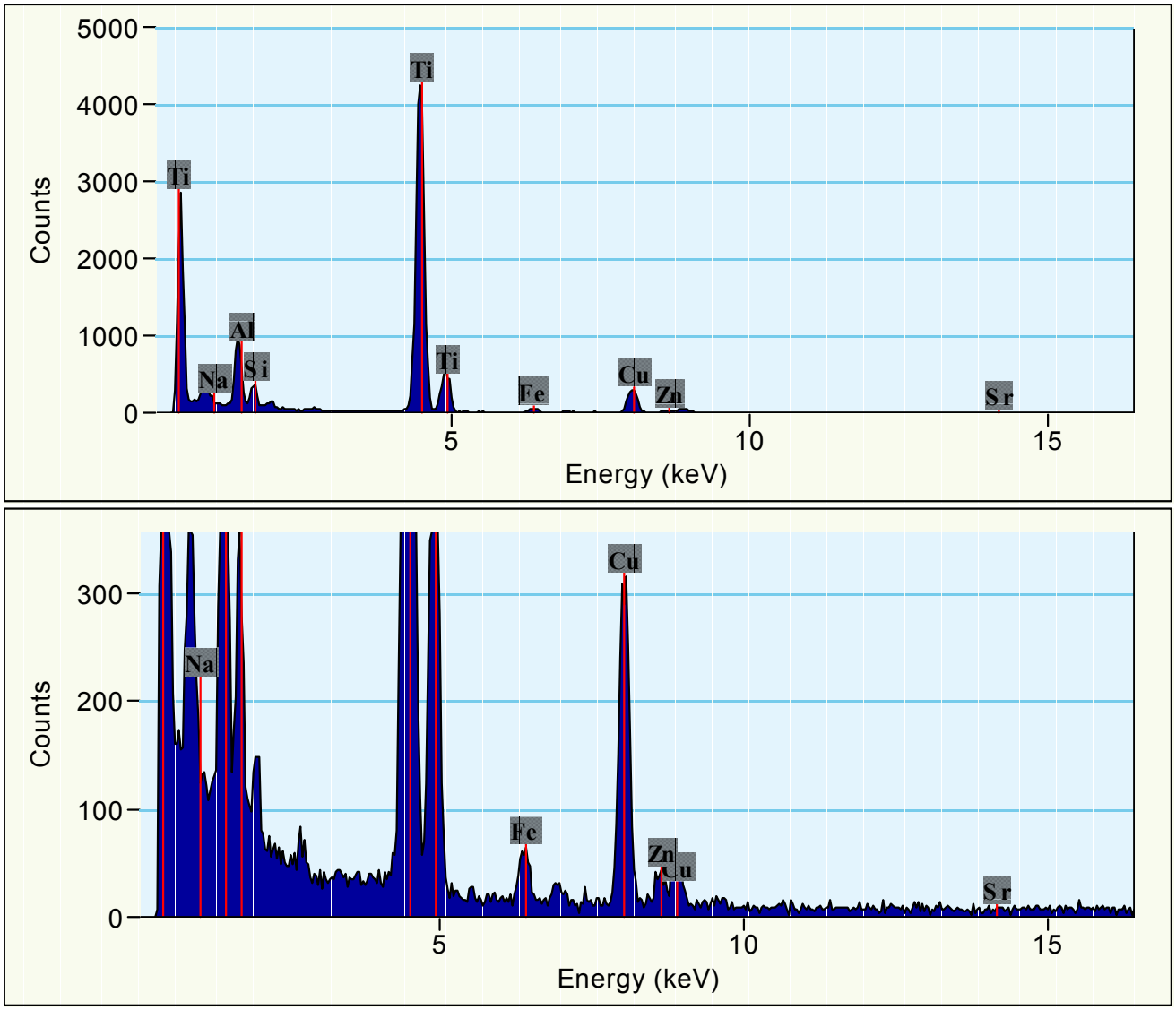

Figure 4.3 EDS spectra taken on the internal (amorphous) regions of the Sr-loaded MST showing the absence of Sr and the presence of Ti, Al, Na, Si, Fe and Zn. The Cu peaks come from the Cu in the sample grid.

NOTE: Due to document format problems, the figure shown above is not a complete reproduction of that presented in the original report document.

4.2 Sample A1, Pu(IV)-loaded MST

Figures 4.4 and **4.5** show the TEM images of the MST in Sample Al [containing Pu originally added as Pu(IV)]. **Figures 4.4** shows a cross-section through an intact MST particle. These images closely resemble those for MST as shown in **Figure 4.1**. The MST particles have an amorphous or nanocrystalline interior surrounded by crystalline "fringes". The outer-fringed layer varies in thickness from approximately 200 to 500 nm. **Figure 4.5** shows a high magnification image of the fringe/interior particle interface. We measured a lattice spacing of 0.63 nm from lattice fringe imaging (data not shown).

A selected area aperture to distinguish the thin, microcrystalline outer fringes from the amorphous or nanocrystalline interior during the electron diffraction studies with Sample A1. The outer fringes produced a pattern typical of weakly oriented microcrystals (**Figure 4.5,** inset). The measured d-spacings appear in **Table 4.2**. We could not identify the crystal structure based on a comparison with literature data. The inner material produced a pattern that might result from disoriented nanocrystalline material (**Figure 4.4, inset**). The texture seen in **Figure 4.4** suggests a very small domain size of a few nm or less.

Figure 4.6 shows a representative EDS spectrum taken from the outer fringe region. The region consists of Ti, O, Na, Al and Ca. The Ca is a contaminant that came from the water used during thin sectioning. Note that Ca did not exist in comparable spectra from the GaTech TEM samples. Calcium exists in all EDS spectra taken from the four samples analyzed at ANL. The Cu peaks in the spectrum result from fluorescence of the Cu support grid. We did not detect plutonium in either the fringe layer or within the interior of the particle with EDS or EELS analysis.

To verify that the thin sections contained Pu, ANL personnel analyzed the grid with alpha spectrometry to measure the total amount of Pu in all the thin sections on the grid. **Figure 4.7** shows the spectrum. The total Pu concentration on the grid equaled 9.58×10^{-7} μg. Each grid contained 15 to 20 sections, with dozens of MST particles within each section. The average thickness of the sections equals 50 nm. These results indicate the Pu is highly dispersed in the sample (i.e., very dilute). Each EELS analysis focuses on only a very small area of one MST particle. Because XAFS results suggest that Pu(IV) distributes on MST in colloidal form, and only a small sample area gets analyzed at high magnification, the ANL personnel carefully examined several MST particles from several different sections in an effort to find Pu colloids in the MST samples.

The calculated Pu concentration in this sample equals 553 mg Pu kg^{-1} (0.05 wt %), which is a loading that falls below the detection limits of both techniques.[18] The XAFS analyses with these samples identified, on average, colloidal Pu.[18] It is possible that the colloids are too small for detection by EDS or ELLS or that there are two types of Pu in the sample: colloidal and highly dilute Pu. If Pu were present in a colloidal form, these techniques could potentially locate the Pu—if it within the thin sections that were analyzed. The thin sections clearly contained a highly dilute form of Pu.

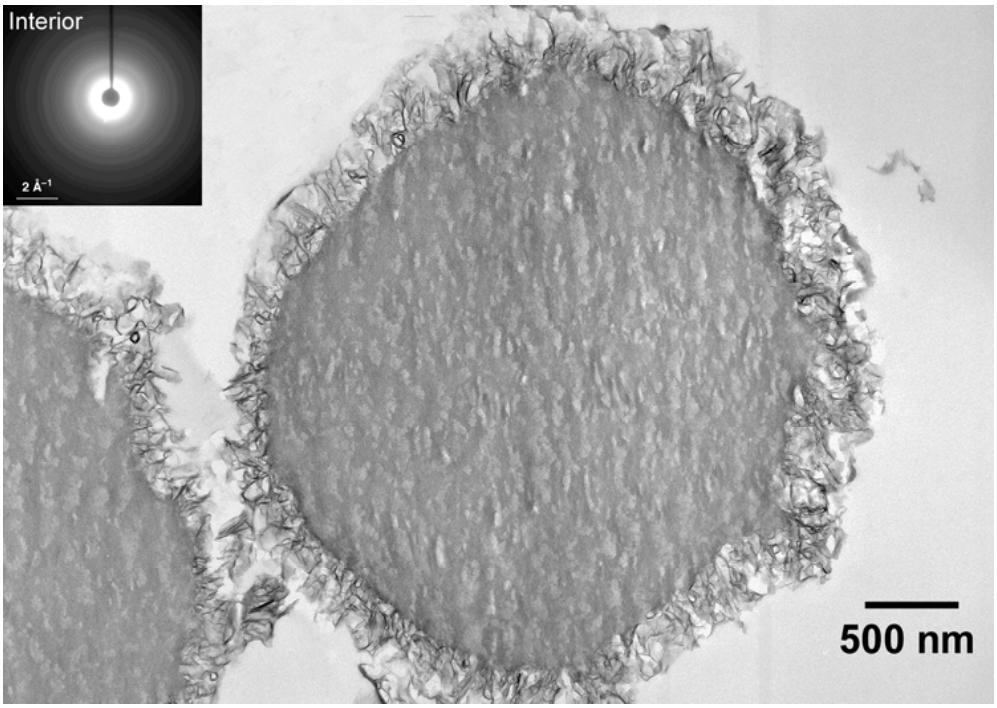

Figure 4.4 Low magnification brightfield TEM images showing the typical morphology of MST particles with corresponding SAED pattern for inner amorphous material.

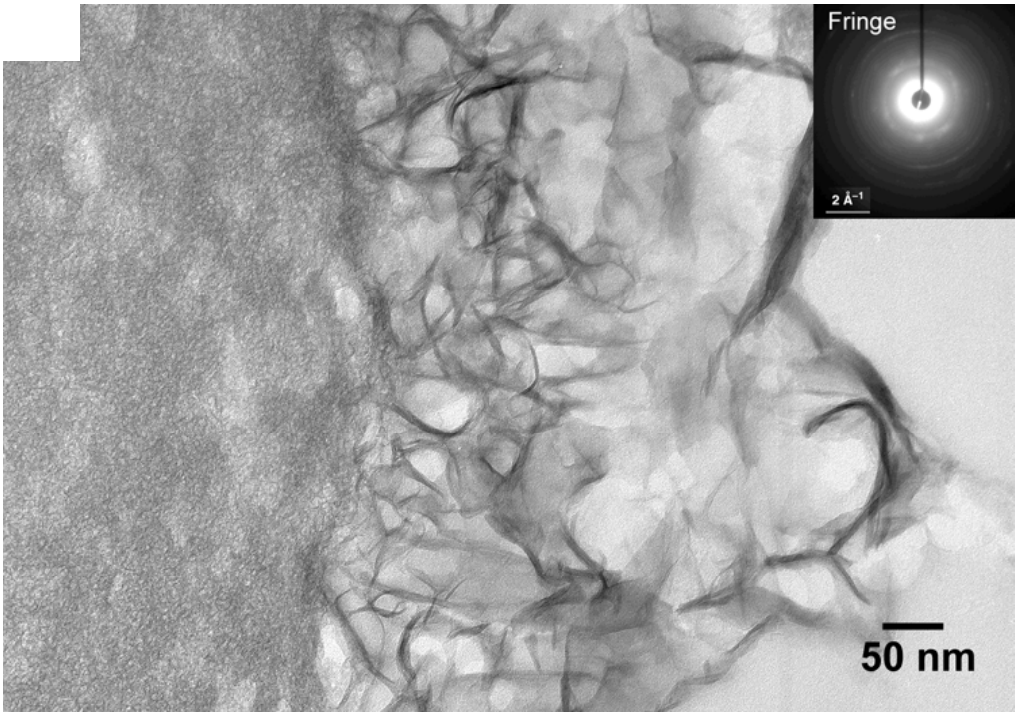

Figure 4.5 High magnification brightfield TEM images showing the typical morphology of MST outer fringe material with corresponding SAED pattern.

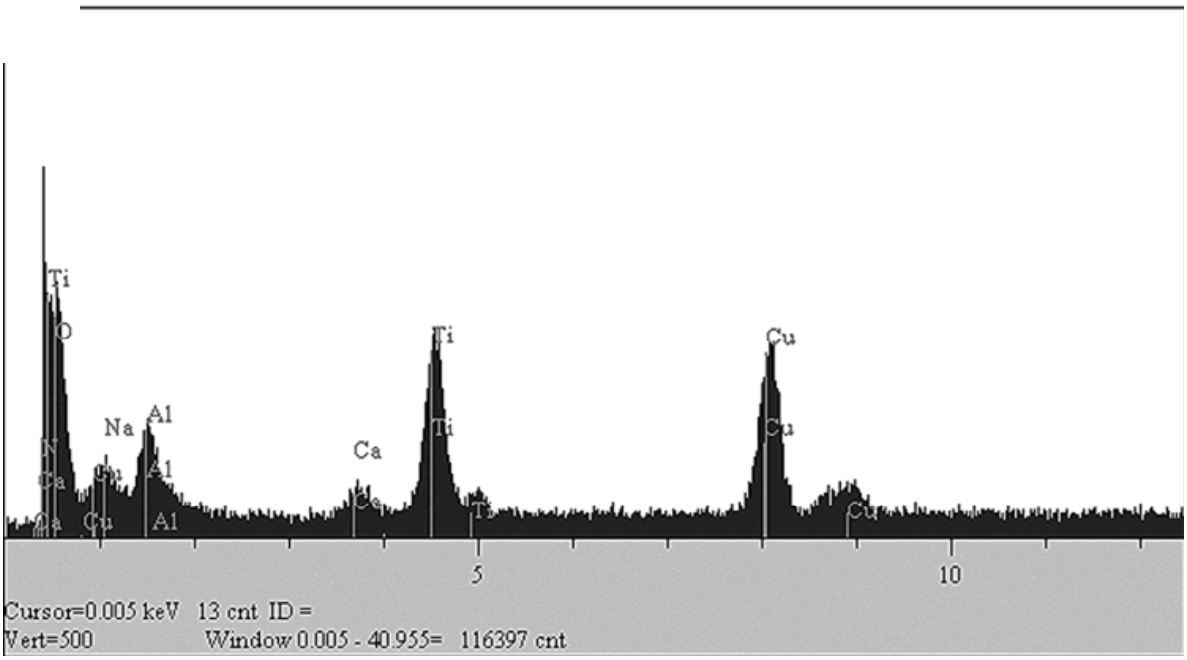

Figure 4.6 EDS spectrum that represents the fringe edges of the Pu-loaded MST samples showing the absence of Pu and the presence of large amounts of Ti, Al, Na, Si and Ca.[c]

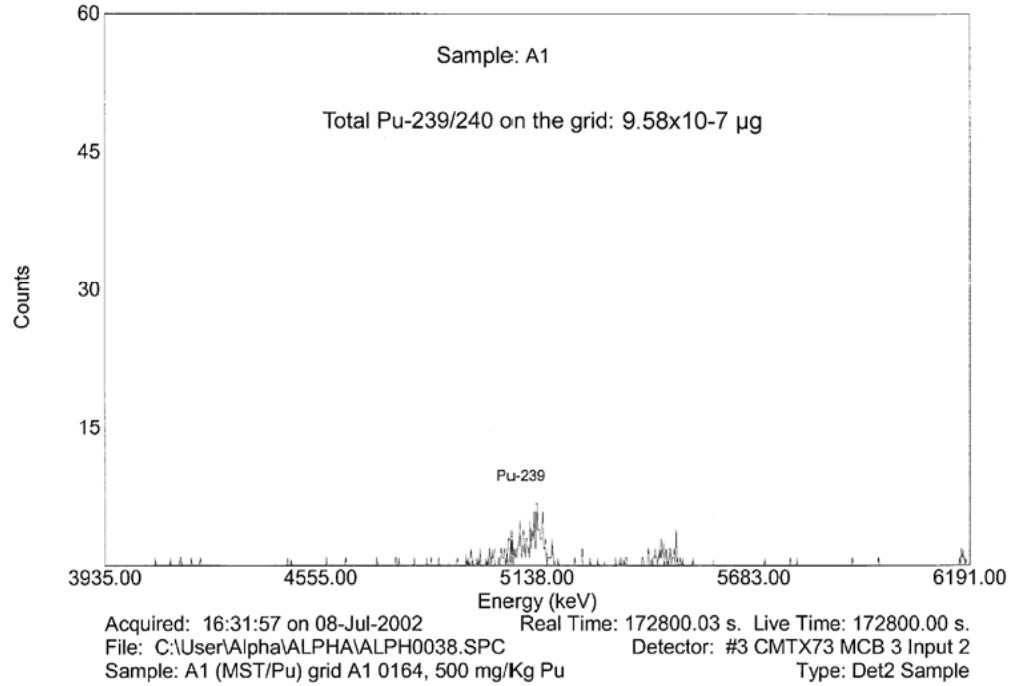

Figure 4.7 Alpha spectroscopic quantification of ^{239}Pu in Sample A1.

[c] The Cu peaks come from the Cu sample grid. The Ca is a contaminant from the thin section preparatory water.

Table 4-2 Electron diffraction from Sample A1, exterior fringes.

Q (1/Å)	d-spacing (Å)
1.68	3.75 ± 0.05
1.73	3.63 ± 0.05
1.84	3.42 (broad)
2.88	2.19 ± 0.03 (faint)
2.98	2.11 ± 0.03
3.30	1.90 ± 0.01
4.18	1.50 ± 0.01
5.37	1.17 ± 0.01

The EELS from the Pu-loaded MST sample A1 failed to detect any Pu, but did include interesting aspects of the Ti-$L_{2,3}$-edges and O K-absorption edge (**Figure 4.8**). The Ti L-edge spectra do not exhibit strong crystal field splitting.[d] Two peaks exist in the Ti absorption edge spectra (**Figure 4.8**), which are indicative of Ti octahedra (TiO_6) groups as opposed to Ti tetrahedral (TiO_4) groups. Little difference exists between the EELS spectra of the interior and exterior (fringe) materials, with the exception of a slightly stronger O K-absorption edge feature of the exterior fringe. This feature may be due to infiltration of the embedding resin. The absence of post-edge structure in the O K-edge EELS spectra indicates of a poorly structured or distorted environment around the O.

4.3 Sample C1, Pu(VI)-loaded MST

TEM examination of Sample C1 [containing Pu originally added as Pu(VI)] shows the same particle morphology and composition as Sample A1 (images not shown). **Figures 4.9** and **4.10** show lattice images. ANL personnel measured lattice spacings of 0.60 and 0.64 nm from these images. Electron diffraction analyses indicate that the d-spacings resemble those found in the Sample A1 (**Table 4-3**). Differences between the two samples (A1 and C1) appear small, although not all of the diffraction spacings observed in A1 occur for this sample. **Figures 4.9** and **4.10** show that the fringes exhibit some terminations, are curved and have a range of basal spacings, which indicates the quite distorted environments for these fibrous materials. This distortion may result from inclusion of interstitial water or hydroxide (OH^-) ions or from the presence of distorted Ti octahedra.

The EDS (data not shown) and EELS analyses did not detect Pu. **Figure 4.11** shows an example of a second-difference EELS in the region of the Pu-N_4 edge and Pu-N_5 edge energy range. The Ti and O speciation in this sample resemble those in Sample A1 as previously discussed.

[d] Crystal field (ligand) splitting is the difference between the highest occupied molecular orbital (HOMO) and the lowest unoccupied molecular orbital (LUMO). The ligand field splitting of metal *d* orbitals is caused by the ligands present, which in this case, the ligand is O.

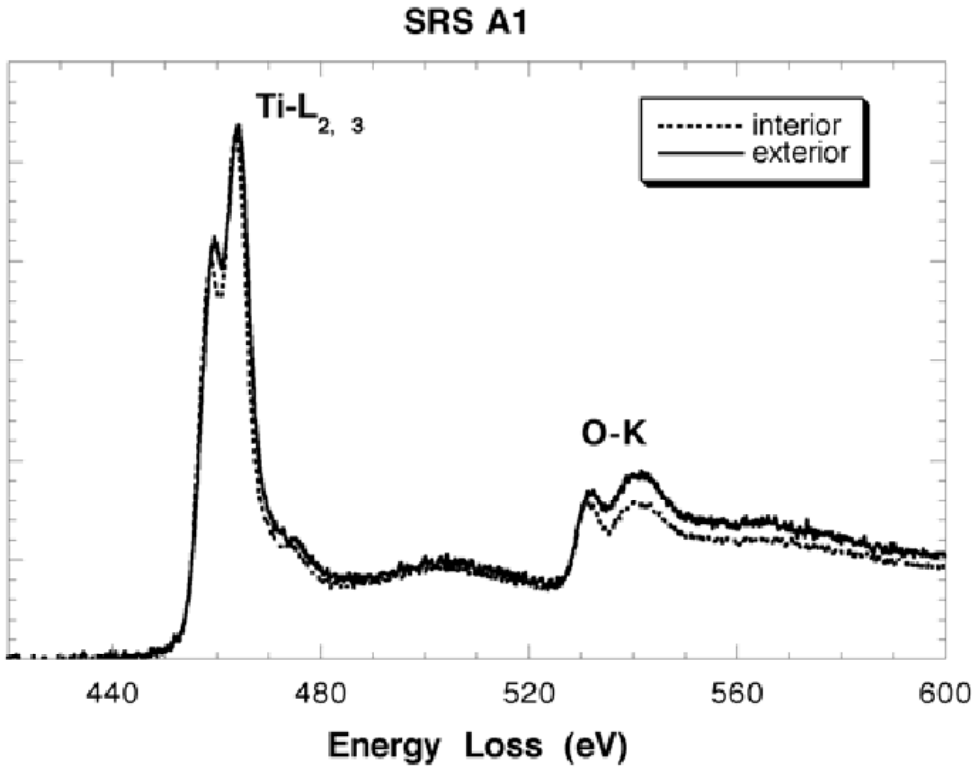

Figure 4.8 Raw Ti $L_{3,2}$-edge and O K-edge spectra for Sample A1.

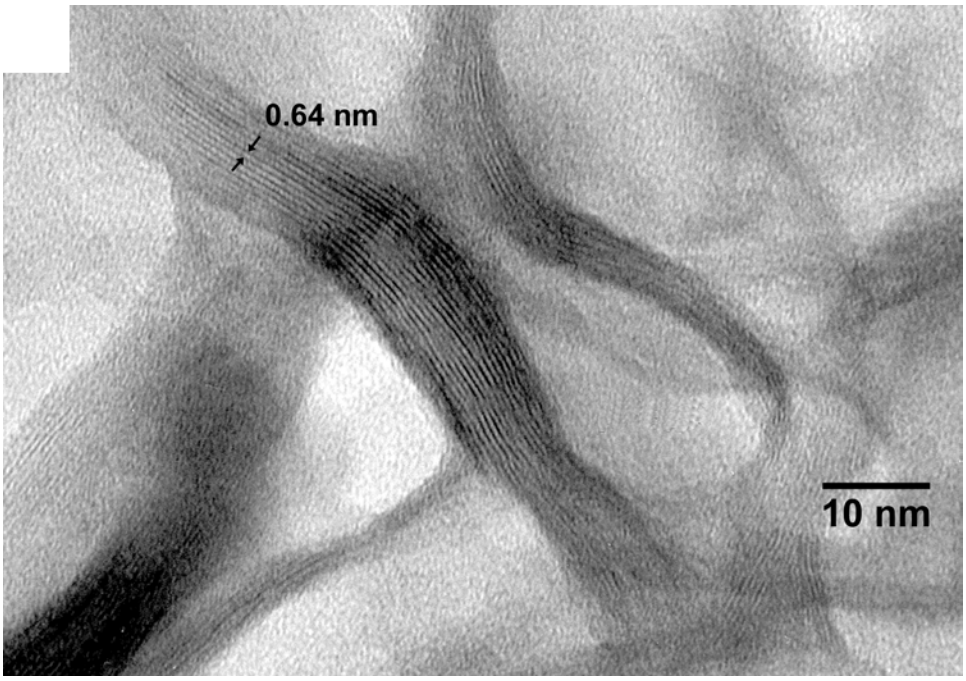

Figure 4.9 High magnification lattice fringe TEM images showing the typical morphology of MST outer fringe material for Sample C1 and the measured basal spacing of 0.64 nm (see arrows).

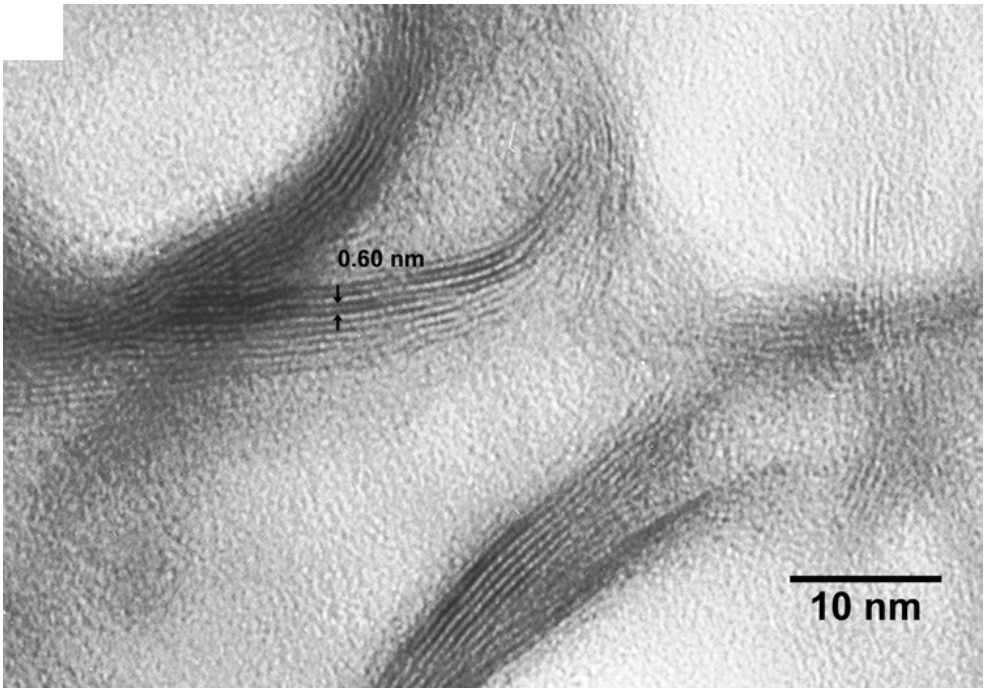

Figure 4.10 High magnification lattice fringe TEM images showing the typical morphology of MST outer fringe material for Sample C1 and the measured basal spacing of 0.6 nm (see arrows).

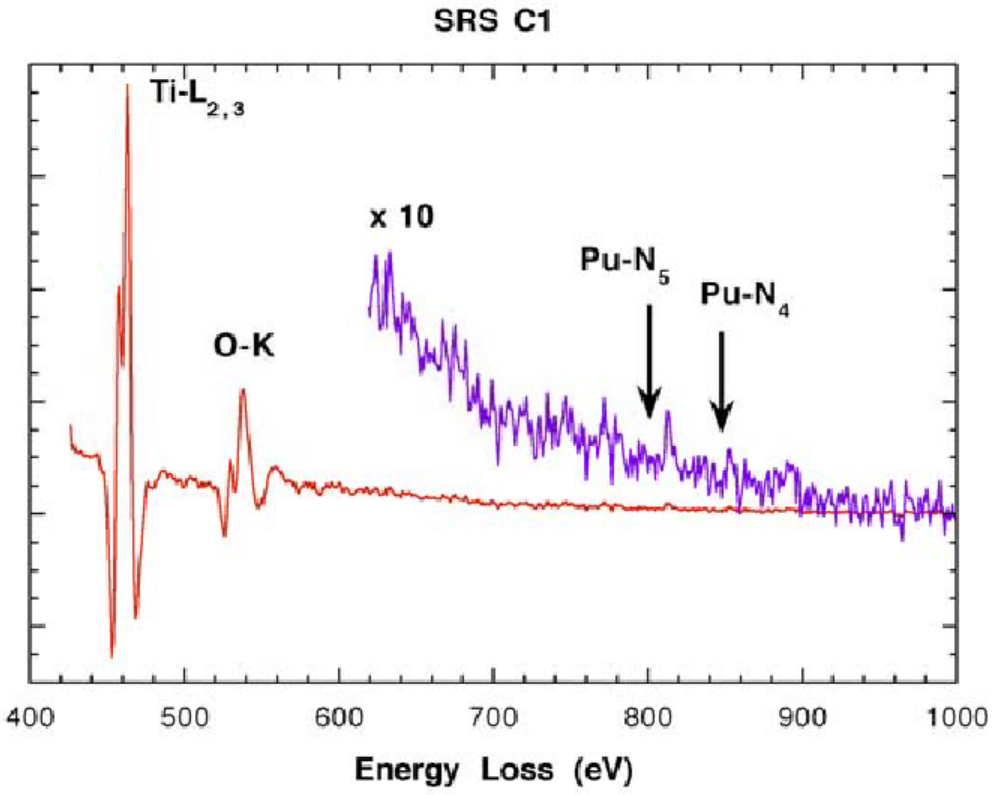

Figure 4.11 Raw Ti $L_{3,2}$-edge and O K-edge spectra for Sample C1 showing the absence of Pu N-edge absorption.

Table 4-3 Electron diffraction from the Sample C1 specimen, exterior fringes.

Q (1/Å)	d-spacing (Å)
1.69	3.72 ± 0.1
1.99	3.16 ± 0.1 (faint)
3.27	1.92 ± 0.03
3.43	1.83 ± 0.03 (faint)
4.16	1.51 ± 0.02
5.32	1.18 ± 0.01

4.4 Sample UMST1, U-loaded MST

TEM examination of Sample UMST1 shows the same particle morphology and composition as that seen in samples Al and C1 (**Figure 4.12**). **Figure 4.12** shows the outer fringe and particle interior interface. **Figure 4.13** shows a lattice plane image with an average measured spacing of 0.62 nm. The lattice spacing of Sample UMST1 varied from 0.55 to 0.67 nm. This range came from measurements taken at six locations on the photographic negative. In the Pu-loaded MST samples, the lattice spacing varied by 0.02 nm. The larger variation in lattice spacing of the U-loaded MST sample could be due to the heterogeneous distribution of atoms or water and might have implications for the mechanism of U sorption on MST. Diffraction measurements from the UMST specimen appear in **Table 4-4**. Differences from the diffraction in the A1 and C1 specimens exceed the instrumental error. Note also the observed spacing of 0.7 nm. Although the level of U in this sample approaches 0.1 wt % (7,500 mg U kg^{-1} MST as determined by sample digestion), EDS and EELS analyses did not detect U.[22]

Table 4-4 Electron diffraction from the Sample UMST1, exterior fringes.

Q (1/Å)	d-spacing (Å)
0.87	7.22 ± 0.1
1.79	3.51 ± 0.05
1.86	3.39 ± 0.1 (broad)
2.06	3.06 ± 0.03
2.60	2.42 ± 0.03
2.90	2.17 ± 0.03 (faint)
3.51	1.79 ± 0.02
4.42	1.42 ± 0.01
5.65	1.11 ± 0.01

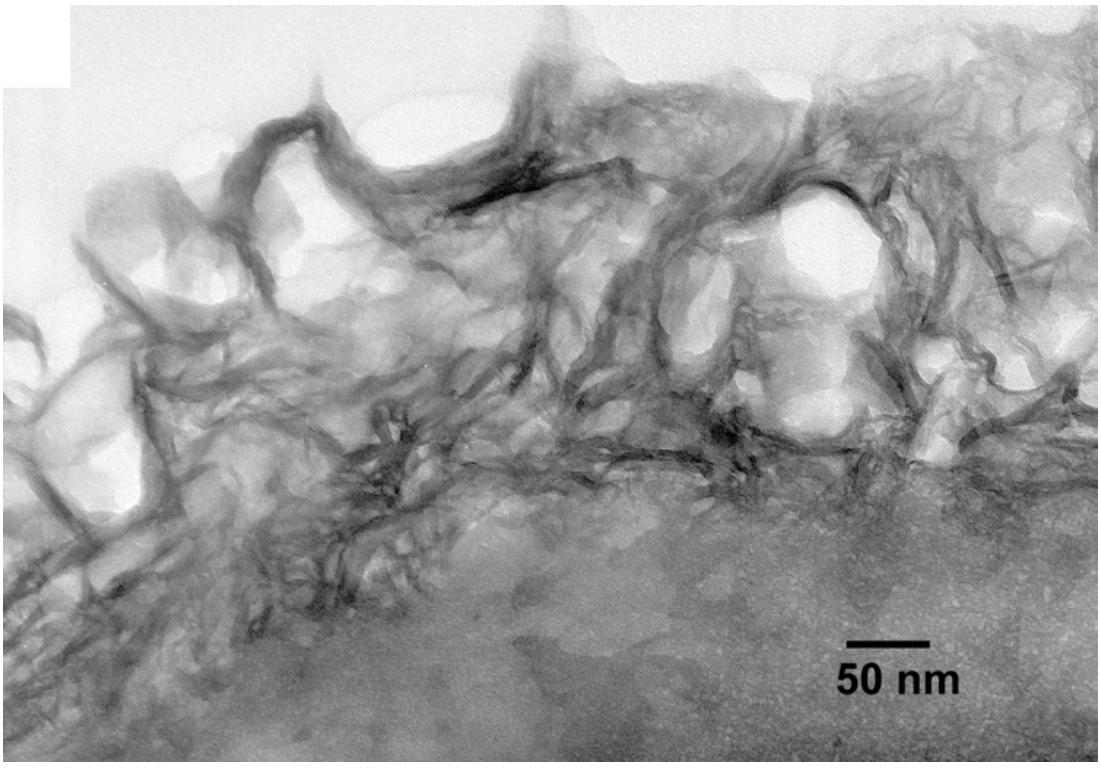

Figure 4.12 TEM image of Sample UMST1 showing the interface between the outer fringe and particle interior.

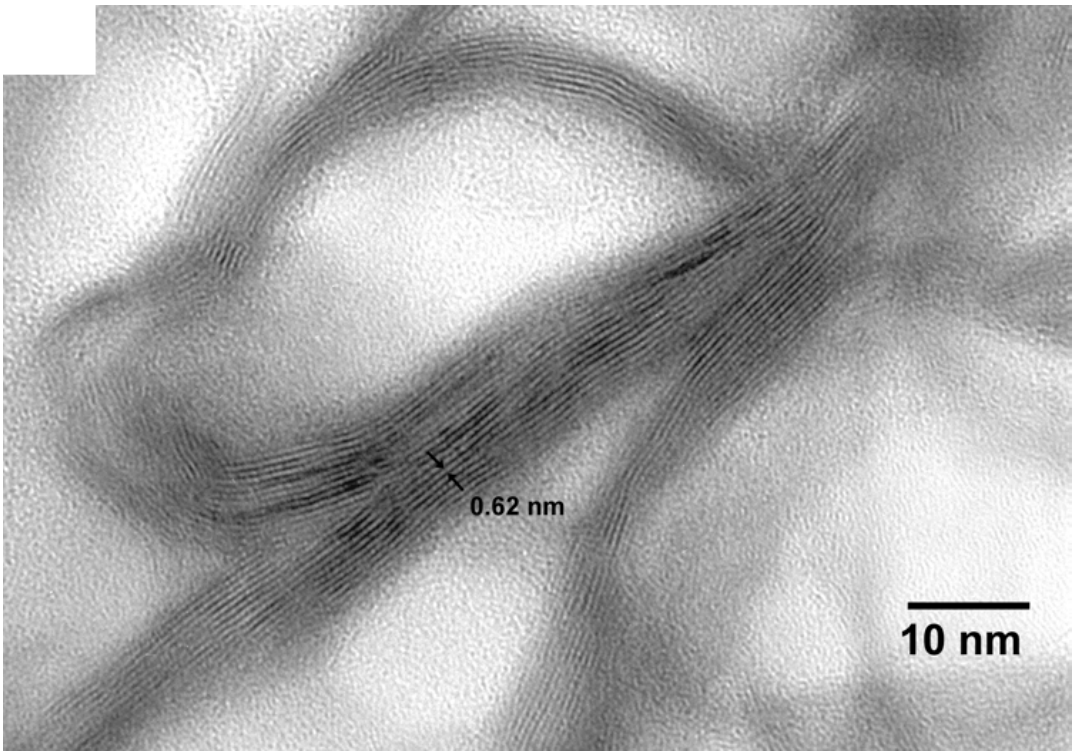

Figure 4.13 High magnification lattice fringe TEM images showing the typical morphology of Sample UMST1 outer fringe material and the measured basal spacing of 0.62 nm (see arrows).

4.5 Sample Manganese Oxide (Non-Radioactive)

We include the results of TEM/SEM analyses performed on permanganate treatment solids without sorbed actinides as an aid in interpreting the results of the Pu-loaded Mn oxide sample (Pu-4B-4h). **Figure 4.14** contains an SEM image of the air-dried sample. The sample, as received, had a paste-like consistency. Personnel smeared some of this material onto an Al support stub and allowed to air dry. The EDS analyses detected Mn, O, Na, Al (Al also exists in the support stub), sulfur (S), and small amounts of silica (Si) and possibly Sr.

The sample proved difficult to section, which complicated the analysis. This difficulty likely occurred because the sample did not dry completely before embedding into the resin. The sample consisted of two compositional morphologies; bundles of tightly-stacked hexagonal platelets arranged in different orientations consisting of Al, O and Mn but relatively high in Al (**Figure 4.15**), and a fine fibrous network consisting of Mn, O and Al but relatively high in Mn. The SAED patterns for the Al rich particles (**Figures 4.15**) resembled chi-alumina (data not shown). The fine fibrous network was almost always associated with the small hexagonal platelets. The hexagonal nature of these particles resembles that of the Mn oxide mineral called birnessite [e.g., $Na_4Mn_{14}O_{27}\bullet 9H_2O_{(s)}$], which exhibits a layered structure (**Figure 2.1**).[23] The Al oxide particles could have formed during the embedding process, which requires heating for 24 hours at 60° C. If the Al were originally present in a amorphous gel form, heating could have converted the gel to an Al oxide such as eta-alumina at temperatures below 100°C.[24] However, our SAED studies indicate that the form of alumina in our sample is the chi form (data not shown) and not the eta form. The following section provides more details on the nature of the Mn solids that form after permanganate reduction.

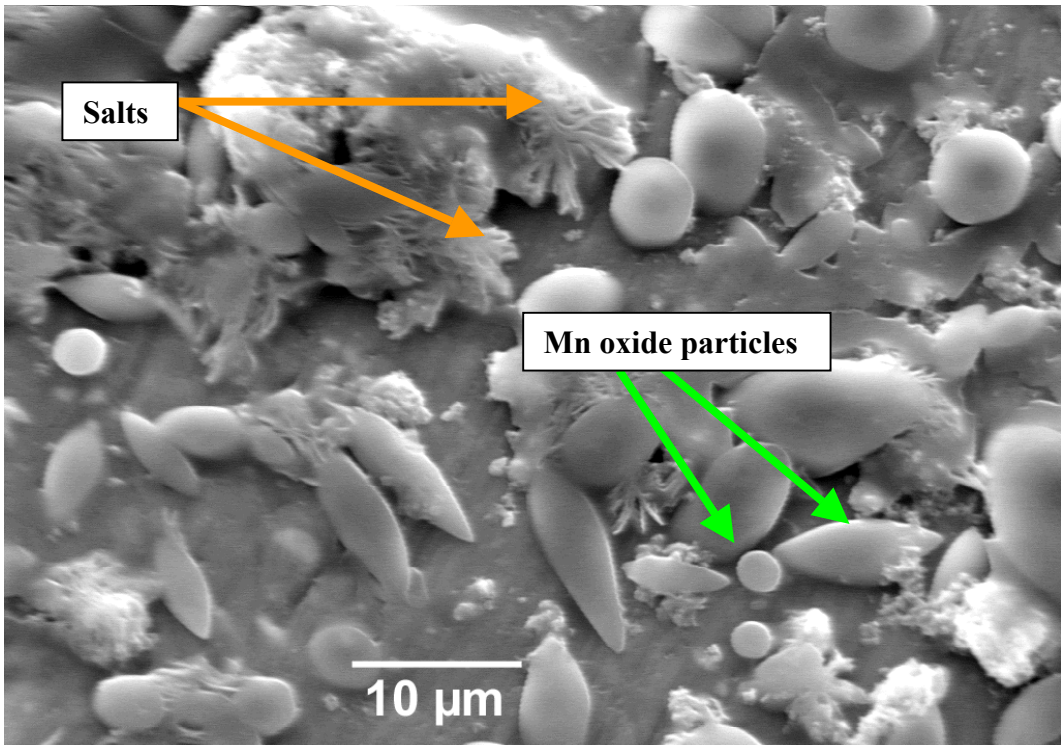

Figure 4.14 SEM image showing the morphologies of the solids that precipitated from 11.6 M Na^+ salt solutions using 0.01M permanganate ion and 0.045 M H_2O_2.

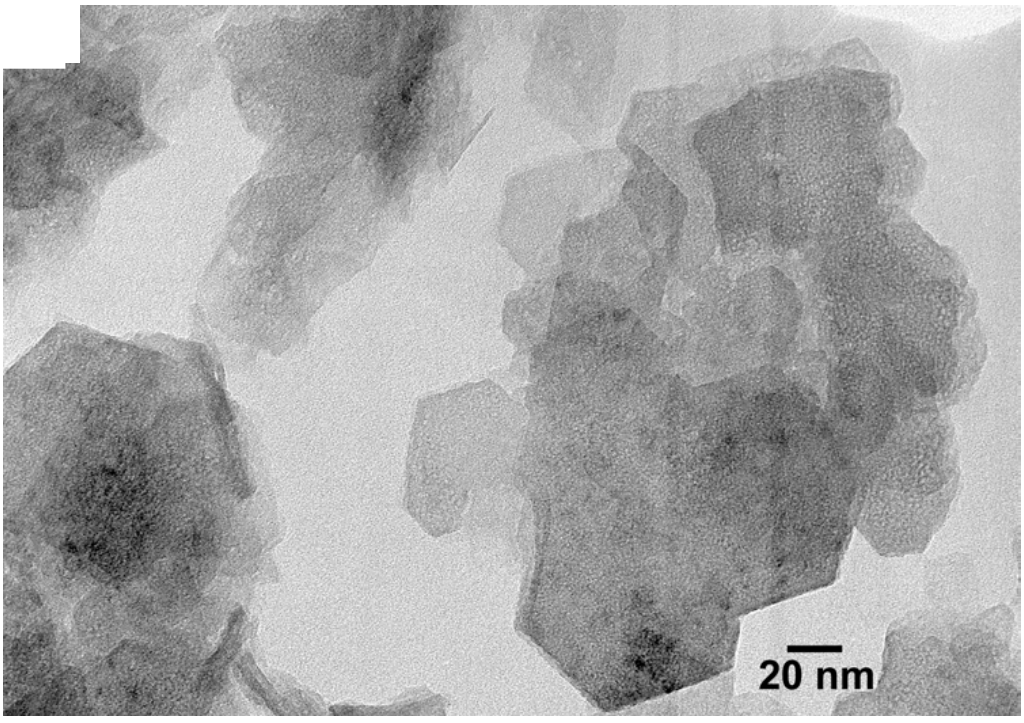

Figure 4.15 TEM micrograph showing the bundles of tightly stacked Al oxide particles in the non-radioactive Mn oxide sample used in the feasibility study.

4.6 Sample Pu-4B-4h (Pu-loaded Mn Oxide)

The TEM images of Sample Pu-4B-4h exhibit compositionally similar morphological features to that of the Mn oxide sample used for the feasibility study. **Figure 4.16** provides a representative low-magnification image of the Mn oxide sample. It consists of a uniform dispersion of small Mn-rich crystallites and large (3 μm) Al oxide particles. **Figure 4.17** displays the EDS spectrum of one large particle that contains Al and O. Examination of the diffraction pattern produced by Al rich areas shows a preferred orientation. These particles generally contain bundles of stacked Al oxide platelets in different orientations. On closer inspection of **Figure 4.16**, one can see sectioning gaps within particles where the orientation of bundles changes. These Al oxide particles could have formed during the embedding process, which requires heating for 24 hours at 60° C. If the Al were originally present in a hydroxide gel form, heating could have converted an Al gel to a crystalline Al oxide.[24] Our X-ray diffraction studies with actinide-free solids that were produced from permanganate reduction identified a Na aluminum oxide as a crystalline phase in addition to nitrate, sulfate and carbonate salts in our Mn oxide samples.[5]

The image in **Figure 4.18** shows the typical microstructure of the smaller dispersed Mn oxide crystallites. **Figure 4.19** contains the EDS spectrum from this area. The crystallites consist mainly Mn and O with small amounts of Al, Si, and Na. The image in **Figure 4.20** shows the small, dispersed crystallites in a different region of the section and under different focusing conditions. This image is "underfocused" to impart more contrast. The crystallites appear surrounded by the same fibrous material seen in **Figure 4.18**. The inset in **Figure 4.20** contains an SAED pattern of a group of the crystallites. The broad rings in the diffraction pattern are typical of amorphous or nanocrystalline material (i.e., it is weakly crystalline) and include contributions from the underlying amorphous carbon support. Hence, we could not make reliable d-spacing measurements. The EDS spectra (in **Figures 4.19** and **4.21**) of the small fibrous-like crystallites in **Figures 4.18** and **4.20** appear essentially identical.

Figure 4.22 shows a non-typical region that contained small beam-stable particles (shown by the arrow in **Figure 4.22**) in association with the fibrous material but not entirely covered by it. These particles consist primarily of Mn, Al and O, as shown in the EDS spectrum in **Figure 4.23**. The Al may also be present in the structure of the Mn oxides (i.e., Al may substitute for Mn in the Mn oxide lattice). **Figure 4.24** shows a nearby region of fibrous material that appears to cover underlying hexagonal platelets. The images suggest that the small crystallites in the sample consist of two compositionally dissimilar morphologies: a "fibrous" particle morphology seen in **Figure 4.18** and an underlying hexagonal platelet morphology, as seen in **Figures 4.20** and **4.22**. Given that the "fibrous" morphology appears to surround the hexagonal platelet morphology, and that normal imaging conditions do not bring this out, we can not reliably estimate how much of each morphology exists. Also note that some Al oxide material occludes the underlying hexagonal Mn-rich bodies.

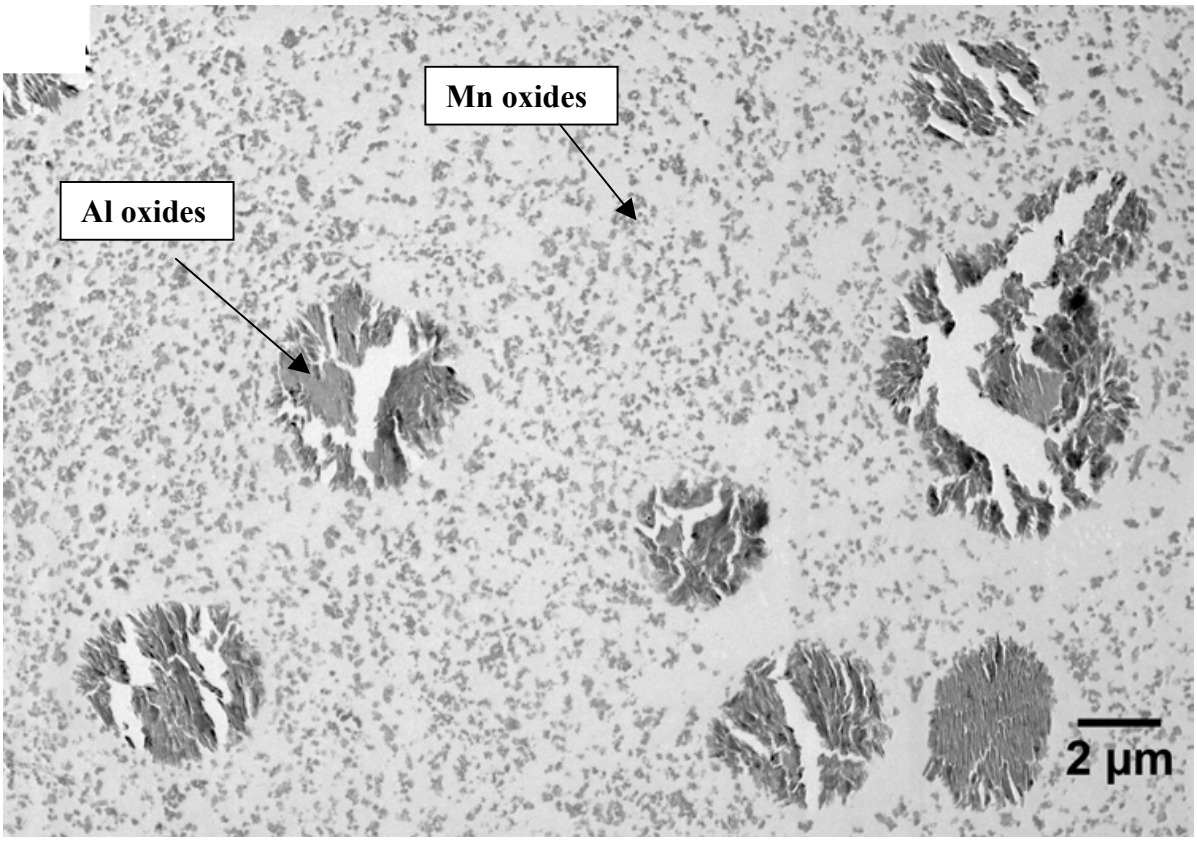

Figure 4.16 Low magnification of Sample Pu-4B-4h showing representative dispersion of small Mn oxide crystallites and large Al oxide particles.

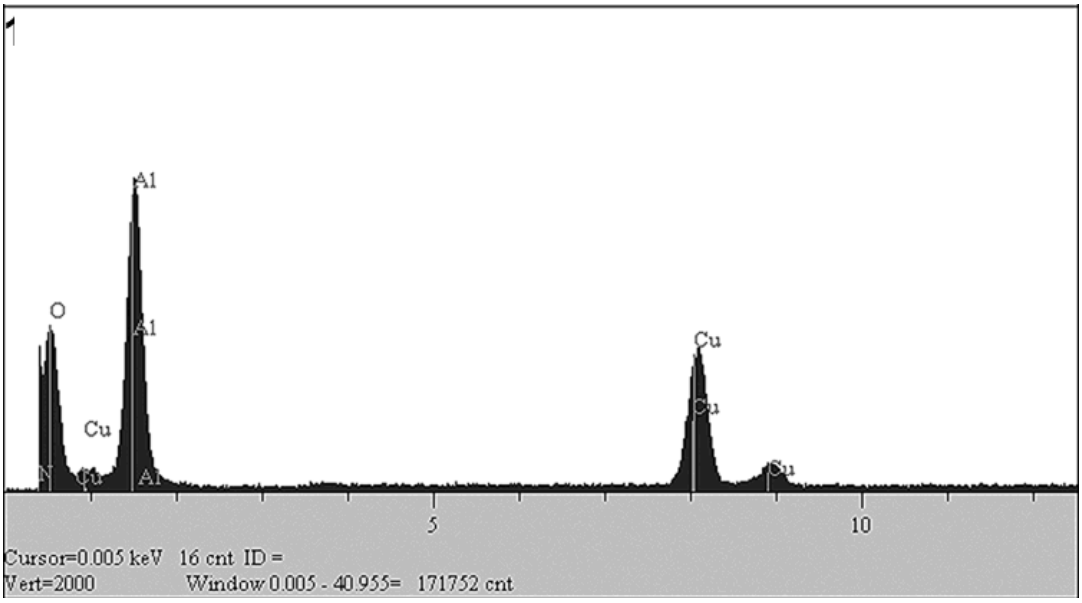

Figure 4.17 EDS spectrum for Sample Pu-4B-4h taken from a large particle in **Figure 4.16**.

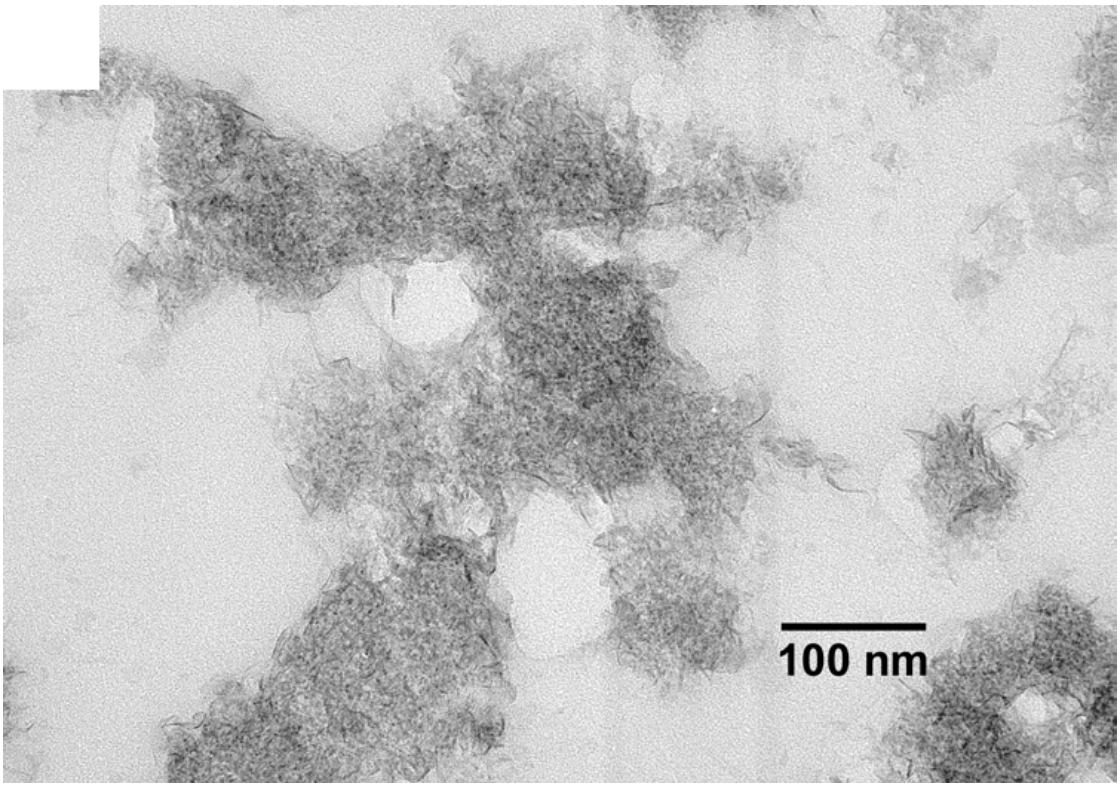

Figure 4.18 TEM micrograph of Sample Pu-4B-4h showing typical microstructure of small dispersed crystallites**.**

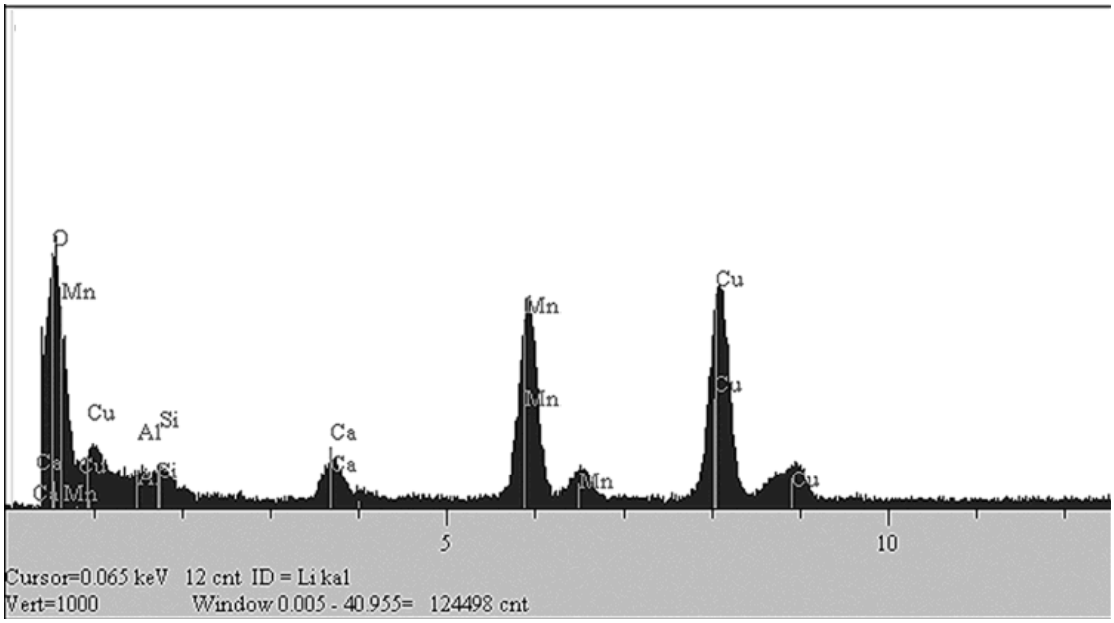

Figure 4.19 EDS spectrum taken from area shown in **Figure 4.18** showing the absence of Pu and the presence of large amounts of O, Mn, and Ca with minor amounts of Al, Si and Na. [e]

[e] The Cu peaks come from the Cu sample grid. The Ca is a contaminant from the thin section preparatory water.

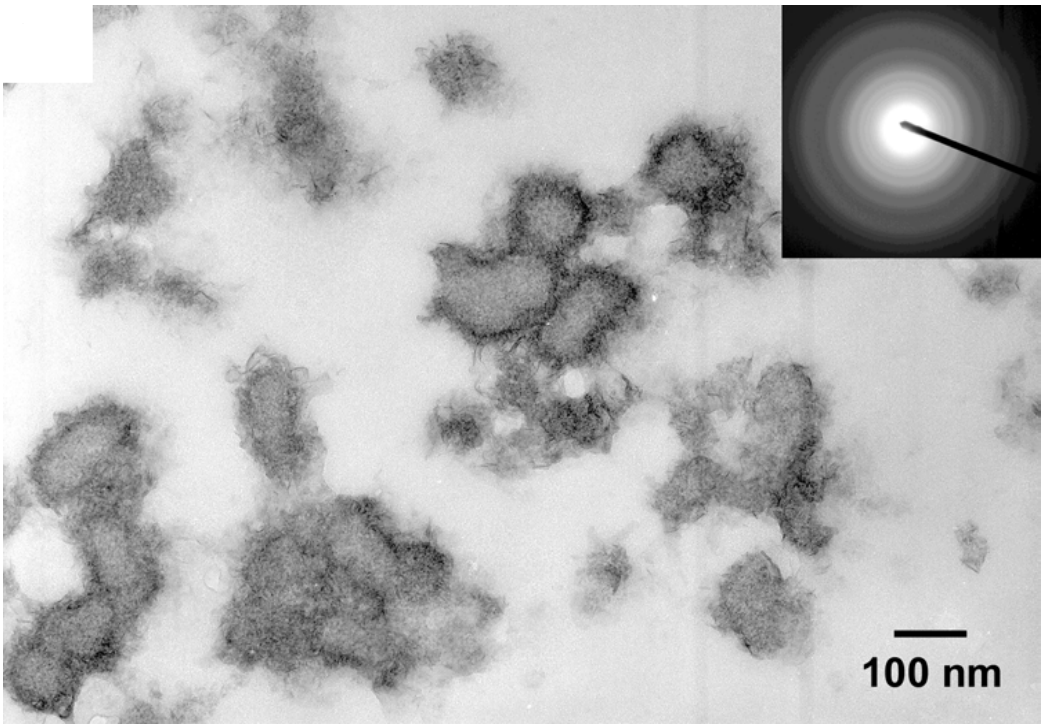

Figure 4.20 TEM micrograph of Sample Pu-4B-4h showing small, dispersed crystallites photographed slightly underfocused to show outline of underlying platelets. Inset shows SAED pattern taken from several crystallites.

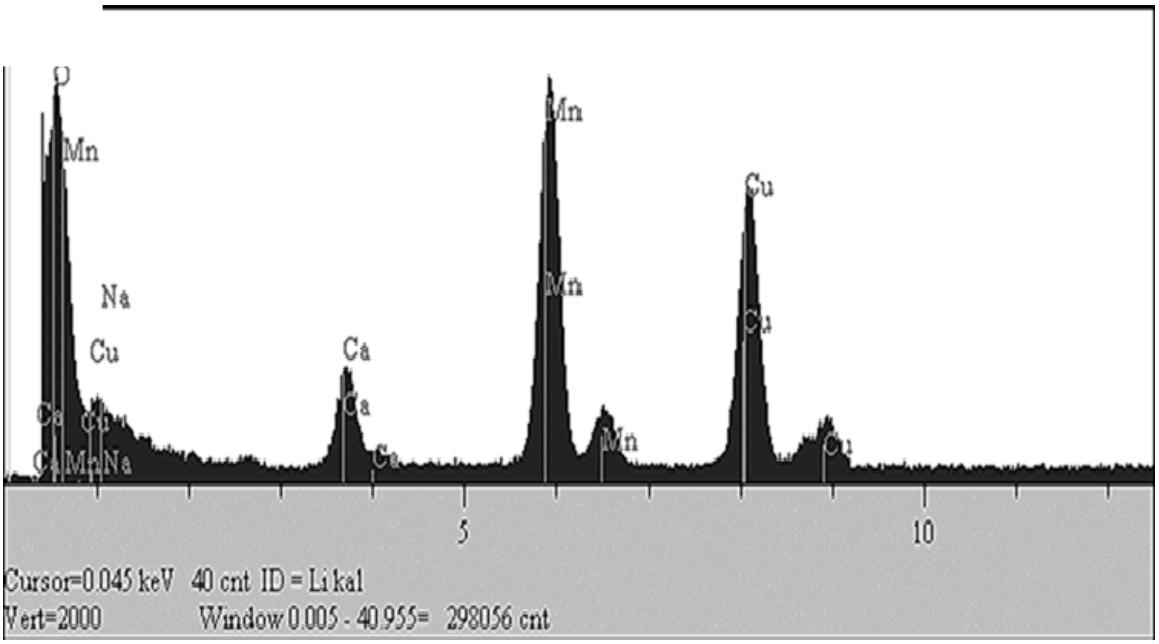

Figure 4.21 EDS spectrum taken from several small Mn oxide crystallites in Sample Pu-4B-4h showing the absence of Pu and the presence of large amounts of O, Mn, Ca, with minor amounts of Al, Na and Si.[f]

[f] The Cu peaks come from the Cu sample grid. The Ca is a contaminant from the thin section preparatory water.

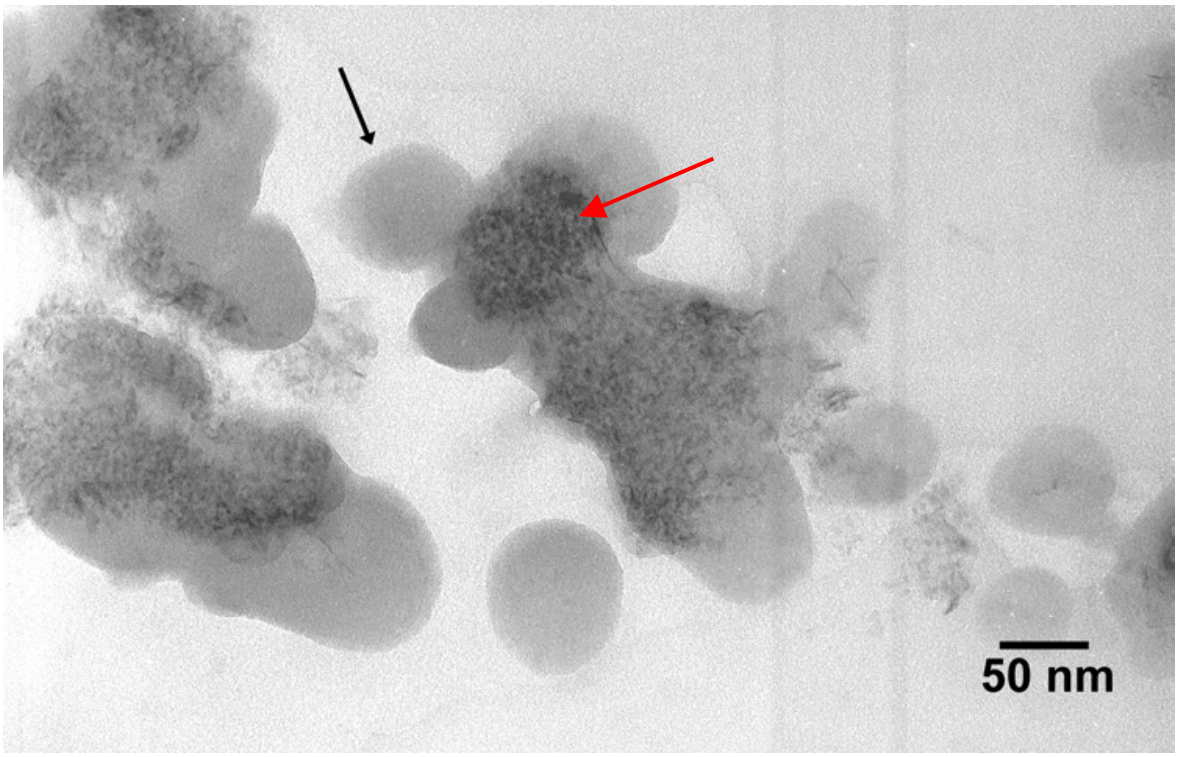

Figure 4.22 TEM micrograph of Sample Pu-4B-4h showing small beam stable particles (black arrow) that rarely existed without "fibrous" material as seen in the particles below it (red arrow).

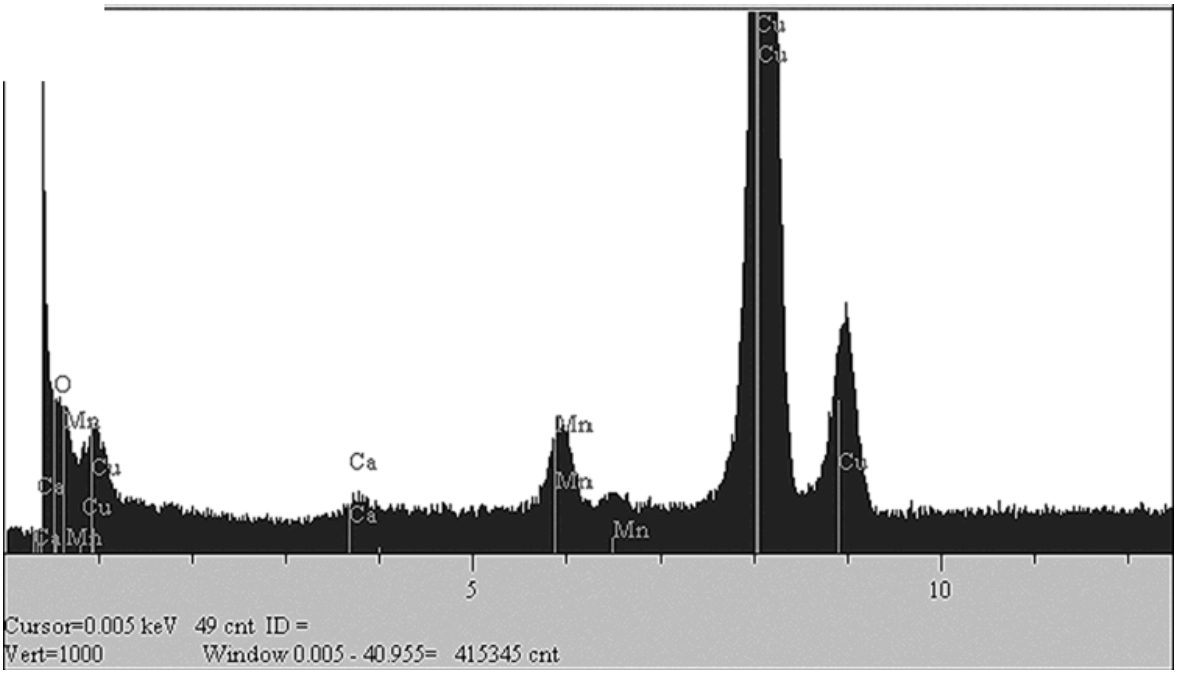

Figure 4.23 EDS spectrum of small Mn aggregate similar to that depicted in **Figure 4.22** showing the absence of Pu and the presence of O, Mn, trace Al, Si and Ca.[g]

[g] The Cu peaks come from the Cu sample grid. The Ca is a contaminant from the thin section preparatory water.

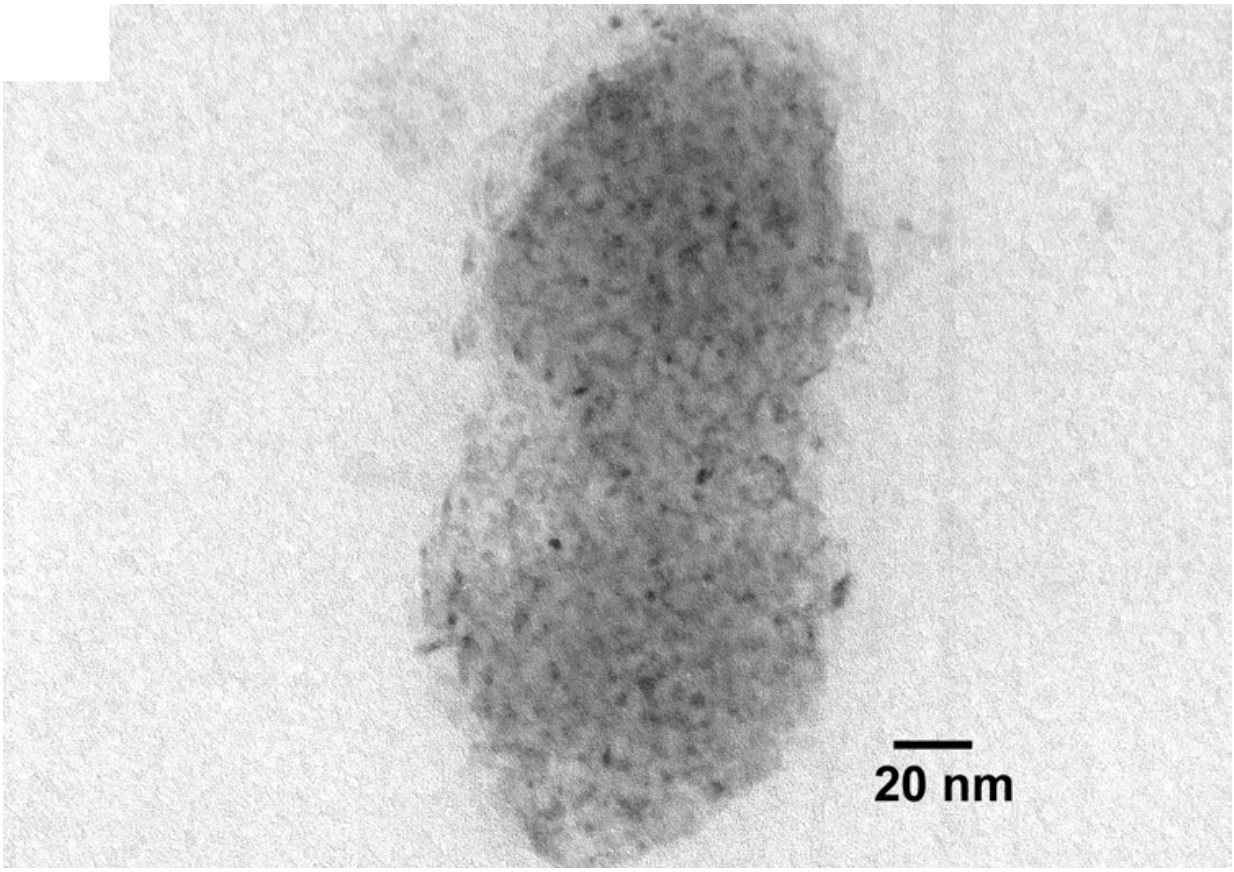

Figure 4.24 TEM micrograph of fibrous material in Sample Pu-4B-4h that appears to cover underlying hexagonal platelets.

Lattice fringes are not clearly recognized in the sample, probably because the orientation and spatial distribution of the crystals limited the number of planes parallel to a zone axis. Regions existed with short-range order, but we can not unequivocally identify these as lattice planes.

The EELS spectra from the Mn oxide specimen reveals interesting structure within the Mn $L_{2,3}$-absorption edges and O-K absorption edge. In **Figure 4.25**, the O K-absorption edge spectrum has a remarkably strong initial onset, with very little post-edge structure. This spectral detail is not typical of Mn oxides[25] and may indicate highly distorted Mn octahedra. An unresolved shoulder exists on the rising edge of the O peak, which may occur due to a large amount of incorporated water or OH^- groups.[26] With background subtraction, the O K-edge spectra for the Pu-loaded Mn oxide sample resemble that of O in MnO_2.[27] The Mn EELS resemble that of a predominantly Mn(IV)-containing Mn oxide material (**Figure 4.26**).[28]

Since we did not detect Pu by EELS, ANL personnel analyzed the grid with alpha spectrometry to determine the total amount Pu on the sample grid. **Figure 4.27** shows the alpha spectrometry plot for $^{239/240}Pu$. The total amount of Pu on the grid equals 2.87×10^{-6} μg. The large amount of Al solids that formed in these samples during treatment effectively "diluted" the amount of Pu (per kg of solid). We prepared these samples to have the highest concentrations of Pu possible to aid in Pu detection by XAFS and TEM techniques as described in Duff et al. (2002) but the final Pu concentration fell well below the expected value.[5] For instance, one targeted Pu loading was ~3,000 mg Pu per kg of MnO_2, a concentration that is suitable for Pu-XAFS studies but based on our experience with actinide-containing solids, we estimate that this particular sample (Test 14) had a level of Pu of about 1,500 mg Pu per kg of MnO_2 instead.[5]

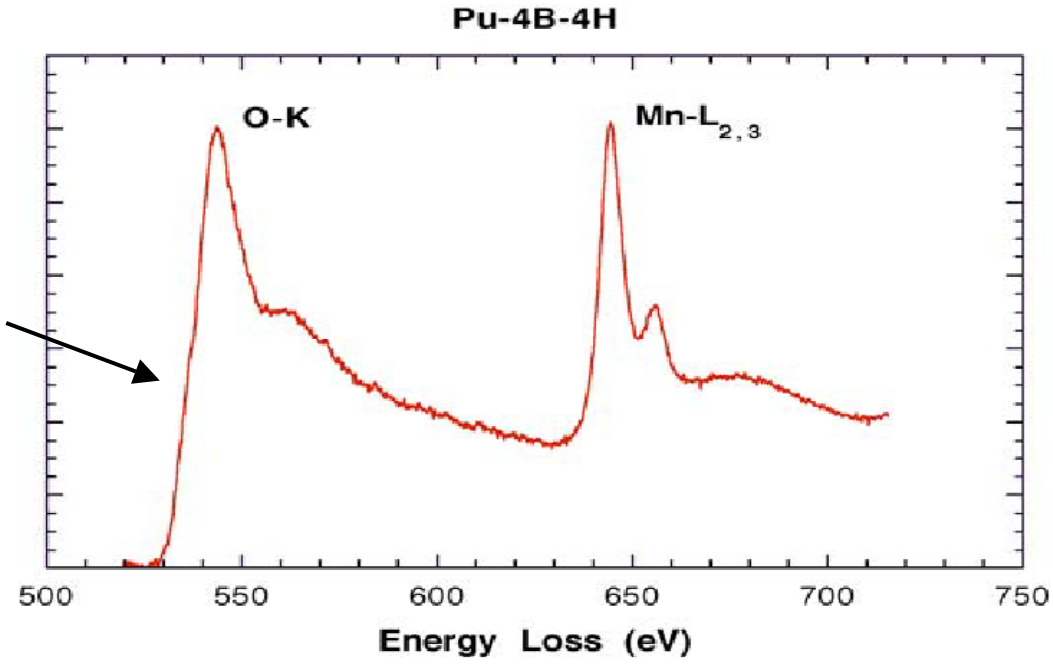

Figure 4.25 Raw EELS spectra for the Sample Pu-4B-4h at the O K-edge and Mn $L_{3,2}$-edges.[h]

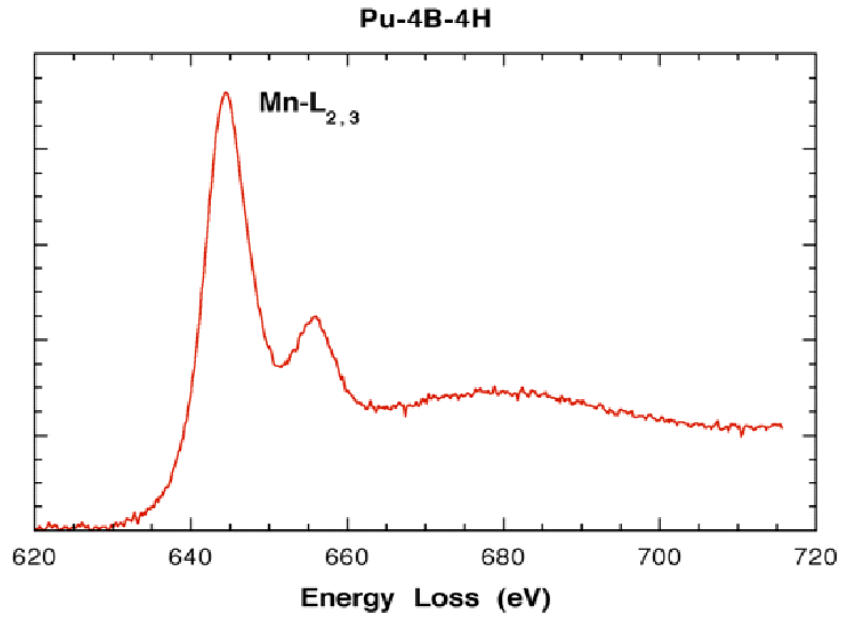

Figure 4.26 Detail of the raw EELS spectra Sample Pu-4B-4h at the Mn $L_{3,2}$-edges.

[h] The arrow denotes the shoulder feature on the low energy side of the white line for the O K-edge spectrum, which is indicative of OH^- or waters of hydration. Background subtractions have not been performed.

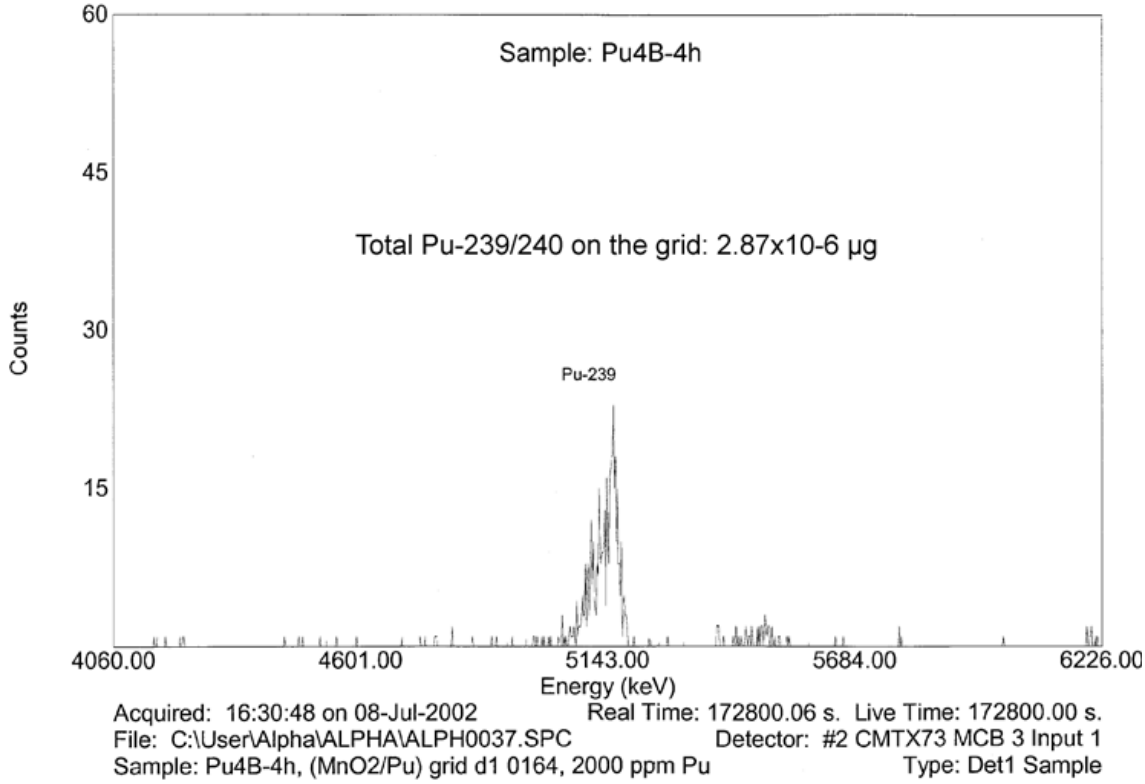

Figure 4.27 Alpha spectroscopic quantification of ^{239}Pu in Sample Pu-4B-4h.

5.0 CONCLUSIONS

5.1 Review of Findings

We used electron microscopy and EELS to characterize candidate sorbent materials from SRTC. The MST particles a microcrystalline, fringed outer-layer about 200 to 500 nm thick that is mechanically continuous with an amorphous, or nanocrystalline, interior. Lattice imaging of the MST fringed outer layer materials shows a highly distorted (curved) substance with average lattice spacings of 0.6 nm. The existence of highly distorted Ti octahedra in MST agrees with previous XAFS work.[18] No substantial morphological differences existed in MST reacted with Sr-, Pu(IV)-, Pu(VI)-, or U(VI)-containing solutions and the unreacted MST. However, the U-loaded MST sample had an average lattice fringe spacing of 0.62 nm, with a range from 0.55 to 0.67 nm. This large range did not exist in the Pu-loaded MST samples. Unfortunately, we not detect on the MST solids by EDS or EELS. These findings do not rule out the possibility that Pu is present as small Pu oxide colloids [as observed in Duff et al. (2001)][18], rather, they indicate that thin sectioned material that was analyzed did not possess this colloidal form of Pu. The sample grids do possess a highly dilute form of Pu, which could not be detected using EELS or EDS. The levels of U in Sample UMST1 proved were lower than the detection limit for the technique.

We examined permanganate treated solids both as non-actinide containing material and as material with Pu. Similar morphological features exist for the actinide-free particles and Pu-loaded materials. Both samples contain two primary morphological populations: a stacked platelet morphology consisting of alumina and a small mixed dispersion of nanocrystalline Mn-rich fibrous and hexagonal materials. We could not obtain a satisfactory diffraction pattern for the Mn oxide particles in the sample and thus can not provide a crystallographic identification of the material. However, the Mn oxide in the sample possesses a hexagonal particle morphology that suggests the sample may contain hexagonal birnessite.[23]

We did not detect plutonium on the permanganate solids by either EDS or EELS. The unexpectedly high levels of Al oxides and other possible solids (of carbonate, sulfate and nitrate)[5] in the samples effectively decreased the targeted Pu-loadings for these samples. Additionally, the low concentrations of Pu observed in the samples compared with the nominal bulk concentrations may also be due to a heterogeneity in the Pu distribution on the TEM sample-size scale. Because the bulk Pu concentration in the samples is at or below 0.1 atomic % (as in **Table 2.1**) would require a large statistical sampling beyond the scope of this project.

5.2 Sample Reactivity to Radionuclide Sorption

The crystalline fringe material on the MST sample and the Mn oxides from the permanganate treatments exhibit a size classification consistent with that of nanoparticles (i.e., colloids). These unique nanostructured components within our samples can be expected to have substantial sorptive properties, higher vapor pressures, and lower melting points in addition to molar free energies that greatly exceed that of larger “macroscopic” particles with similar chemical make-ups.[29] Predictions of the amount of radionuclide sorption on a per surface area

basis based on studies with macroscopic particles are likely to highly underestimate the sorptive capacity of these nanoparticles.

5.3 Process Optimization

An improvement to MST sorbent design could include the synthesis of particles with a higher fringe-to-amorphous component ratio. If possible such a modification could increase radionuclide removal rates. Work should be conducted to evaluate the use of MST particles with higher fringe-to amorphous contents for radionuclide removal and filtration.

During permanganate treatment, the precipitation of Al oxides coincides with Mn oxide precipitation. Studies at SRTC with actual wastes from Hanford show that the Mn solids that form upon permanganate addition in the absence of radionuclides do not exhibit strong radionuclide decontamination after precipitation.[30] These TEM studies indicate that the reactive surfaces of the Mn oxides are occluded by Al oxides and other salts— a process that may physically limit the access of radionuclides to the Mn oxides. (Note that Al-rich Mn oxide and salt material is observed in the two types of Mn particle morphologies observed in our permanganate samples). An optimization of permanganate treatment could include the study the influence of ionic strength on radionuclide removal kinetics.

Additional TEM work with samples containing higher actinide loading is recommended. The use of a more powerful TEM instrument, such as one with a higher accelerating voltage, state-of-the art imaging capability, scanning transmission capability in addition to EELS capabilities is also recommended.

6.0 ACKNOWLEDGMENTS

The authors thank H. Harmon (PNNL), P. Suggs (DOE), J. T. Carter (WSRC) and F. Fonduer (SRTC) for their assistance, support and ideas. Betty Croy, K. Prettel and N. Gregory (all of SRTC) assisted with the preparation of the permanganate and MST samples. Mira Malek, P. Woller, and R. Boyce (all of SRTC) performed the ICP-MS analyses. Rene Johnson and J. Russell (both of WSRC) are acknowledged for their help with shipping these samples. Connie Pierce (WSRC) provided health physics support in the laboratory.

7.0 REFERENCES

[1] Duff, M. C., Hobbs, D. T. and Fink, S. D. (2002). Permanganate Treatment Optimization Studies for Strontium and Actinide Removal from High Level Waste Simulants, WSRC-TR-2002-0027, January 14, 2002.

[2] Barnes, M. J., Hobbs, D. T., Duff, M. C. and Fink, S. D. (2002). Permanganate Reduction of Savannah River Site Actual Waste Samples for Strontium and Actinide Removal. WSRC-TR-2002-00048, Rev. 2 August 12, 2002.

[3] Hobbs, D. T., Blume, M. S. and Thacker, H. L. (2000). Screening Evaluation of Sodium Nonatitanate for Strontium and Actinide Removal from Alkaline Salt Solution. WSRC, WSRC-TR-2000-00361, Aiken, SC.

[4] Leinonen, H. and Lehto, J. (1998). Sodium-hydrogen ion exchange in sodium titanate $Na_4Ti_9O_{20}$ xH_2O. *Radiochem*. **40**, 503-506.

[5] Duff, M. C., Hunter, D. B., Hobbs, D. T., Jurgensen, A. and Fink, S. D. (2002). Characterization of Sorbed Plutonium, Neptunium, Strontium on Manganese Solids from Permanganate Reduction. WSRC-TR-2002-00366, Rev. 0, Sept. 19, 2002.

[6] Morgenstern, A. and Choppin, G. R. (2002). Kinetics of the oxidation of Pu(IV) by manganese dioxide. *Radiochim. Acta* **90**, 69-74.

[7] Crespo, M. T., Gascon, J. L. and Acena, M. L. (1993). Techniques and analytical methods in the determination of uranium, thorium, plutonium, americium and radium by adsorption on manganese dioxide. *Sci.Tot.Environ*. **130**, 383-391.

[8] Shen, Y. F., Zerger, R. P., DeGuzman, R., Suib, S. L., McCurdy, L., Potter, D. I. and O'Young, C.-L. (1993). Octahedral molecular sieves: Synthesis, characterization and applications. *Science* **260**, 511-515.

[9] Dyer, A., Pillinger, M., Newton, J., Harjula, R., Moller, T. and Amin, S. (2000). Sorption behavior of radionuclides on crystalline synthetic tunnel manganese oxides. *Chem. Mater.* **12**, 3798-3804.

[10] Chukrov, F. V., Sakharov, B. A., Gorshkov, A. I., Drits, V. A. and Dikov, Yu. P. (1985) Crystal structure of birnessite from the Pacific Ocean. *Inst. Geol. Rev.* **27,** 1082-1088.

[11] Behrens, E. A., Sylvester, P. and Clearfield, A. (1998). Assessment of a sodium nonatitanate and pharmacosiderite-type ion exchangers for strontium and cesium removal from DOE waste simulants. *Environ. Sci. Technol*. **32**, 101-107.

[12] Sun, X., Ma, C., Zeng, L., Wang, X. and Li, H. (2002). A facile method to prepare layered manganese oxides with large interplanar spacing. *Mater. Res. Bull.* **37**, 331-341.

[13] Liu, Y. P., Qian, Y. T., Zhang, Y. H., Zhang, M. W., Wang, C. S. and Yang, L. (1997). γ-ray radiation preparation and characterization of nanocrystalline manganese dioxide. *Mater. Res. Bull.* **32**, 1055-1062.

[14] Quigwen, L., Yiming, W. and Guoan, L. (1999). pH-response of nanosized MnO_2 prepared with solid state reaction route at room temperature. *Sensors Actuators* **B 59**, 42-47.

[15] Youn, S. G., Lee, I. H., Yoon, C. S., Kim. C. S. Kim, C. K., Sun, Y.-K., Lee, Y.-S. and Yoshio, M. (2002). Microstructure and cycling behavior of $LiAl_{0.1}Mn_{1.9}O_4$ cathode for lithium secondary batteries at 3 V. *J. Power Sources* **108**, 97-105.

[16] Kumar, V. (1999). Solution-precipitation of fine powders of barium titanate and strontium titanate. *J. Am. Ceram. Soc.* **82**, 2580-2584.

[17] Duff, M. C., Hunter, D. B., Hobbs, D. T. and Fink, S. D. (2001). Characterization of Sorbed Strontium on Monosodium Titanate. WSRC-TR-2001-0245, June 25, 2001.

[18] Duff, M. C., Hunter, D. B., Hobbs, D. T., Barnes, M. J. and Fink, S. D. (2001). Characterization of Sorbed Uranium, Plutonium and Neptunium on Monosodium Titanate. WSRC-TR-2001-00356, Sept. 19, 2001.

[19] Edgerton, R. F. (1996). Electron Energy Loss Spectroscopy in the Transmission Electron Microscope, 2nd. ed. Plenum, New York, NY.

[20] Fortner, J. A. and Buck, E. C. (1996). The chemistry of the light rare-earth elements as determined by electron energy loss spectroscopy. *Appl. Phys. Lett.* **68**, 3817-3819.

[21] Langhammer, H. T., Müller, T., Felgner, K.-H. and Abicht, H.-P. (2000). Influence of strontium on manganese-doped barium titanate. *Materials Lett*. **42**, 21-24.

[22] Duff, M. C., Hunter, D. B., Hobbs, D. T., Barnes, M. J., Fink, S. D., Dai, Z. and Bradley, J. P. (2002). Mechanisms of Sr and U(VI) Removal from High-level Radioactive Waste Simulant Solutions by the Sorbent Monosodium Titanate. to be submitted to *Environmental Science and Technology.*

[23] McKenzie, R. M. (1989). Manganese oxides and hydroxides. *In* Minerals in Soil Environments (second Ed.) Soil Science Soc. of America, Madison, WI, 439-441.

[24] Wefers, K. and Misra, C. (1987). Oxides and Hydroxides of Aluminum. Alcoa Laboratories. Alcoa, TN.

[25] Wang, Z. L., Yin, J. S., Mo, W. D. and Zhang, Z. J. (1977). In-situ analysis of valence conversion in transition metal oxides using electron energy-loss spectroscopy. *J. Phys. Chem. B* **101** (35) 6793-6798.

[26] Wirth, R. (1997). Water in minerals detectable by electron energy-loss spectroscopy EELS. P*hys. Chem. Minerals* **24,** 561-568.

[27] Moltaji, H. O., Buban, J. P., Zaborac, J. A. and Browning, N. D. (2000). Stimulating the oxygen K-edge spectrum from grain boundaries in ceramic oxides using the multiple scattering methodology. *Mircon* **31**, 381-399.

[28] Splide, M. N., Brearley, A. J. and Papike, J. J. (2001). Mn oxide materials from a terrestrial cave environment: Biomarkers for the search for life on Mars? *Lunar Planetary Science* XXXII, p. 1454.

[29] Zhang, H., Penn, R. L., Hammers, R. J. and Banfield, J. F. (1999). Enhanced adsorption of molecules on surfaces of nanocrystalline particles. *J. Phys. Chem*. B **103,** 4656-4662.

[30] Wilmarth, W. R. (1999). Strontium/TRU Scoping Tests. WSRC-NB-1999-00112, pp. 37-39 and 62.